scientific reports

OPEN

# An unresolved SPH-DEM model for simulation of ductile and brittle surface erosion by abrasive water-jet (AWJ) impact

Ran Yu, Guannan Hao✉, Weijia Yang & Zhinan Li

**The abrasive water-jet (AWJ) erosion process involves the complex interaction between fluid medium, abrasive particles and solid material, which brings great challenges to the establishment of numerical model. Because traditional grid-based methods are not suitable for the problems of local deformation and material removal, the meshfree method smoothed particle hydrodynamics (SPH), based on the unresolved coupling and the discrete element method (DEM), is adopted to establish the model for AWJ study. The fluid medium is treated as a weakly compressible viscous liquid, the solid material is treated as an elastic-plastic material, and the abrasives are treated as rigid bodies. The fluid and solid phases are discretized with SPH particles, and the abrasives are described with DEM particles. The Johnson-Cook (J-C) and Johnson-Holmquist-II (JH-2) constitutive models are used to describe the stress-strain behavior of ductile and brittle materials, respectively. The effectiveness of the numerical model is further verified by AWJ impact experiments. The plastic deformation and cumulative failure characteristics of ductile materials, and the crack formation and propagation characteristics of brittle materials are systematically analyzed. The results provide insight for the AWJ research and lay a foundation for investigation of other complex fluid-particle flow in a numerical way.**

**Keywords** SPH-DEM coupled method, Abrasive water-jet, Fluid–particle-solid interaction, Surface erosion, Ductile and brittle materials

Abrasive water-jet (AWJ) cutting technology is a type of machining technology developed on the basis of pure water-jet cutting technology. With the same water pressure, the erosion ability of AWJ is much greater than that of pure water-jet[1]. AWJ technology is initially used in the mining industry, and plays an important role in coalbed methane extraction and gas prevention operations. Since the 1980s, AWJ technology has been widely used in the machining field. Compared with traditional cutting tools and new thermal cutting technologies such as laser beam, electron beam and plasma, AWJ cutting technology has the advantages of no heat affected zone, low processing stress, high quality of slit surface, wide processing range and clean and environmental protection, which has been widely used in cutting operations of metals, rocks, ceramics and composite materials[2,3].

In early stage of AWJ technology application, erosion experiment is the main research method. However, the complex interaction between different jet parameters makes the experimental process time-consuming and expensive. In addition, due to the short impact duration and small erosion area, it is difficult to directly observe the plastic deformation and material removal during impact process, which makes the study of AWJ erosion mechanism quite difficult. Therefore, in the past two decades, various numerical methods have been widely developed and used to predict the erosion performance and reveal the erosion mechanism.

The traditional grid-based method of Finite Element Method (FEM) was initially used to describe the stress-strain behavior of the solid material, and there were various ways to describe the water-jet. In the Coupled Eulerian Lagrangian Method (CEL), the AWJ was modelled by Euler grid, and the solid phase was modelled by FEM based on Lagrangian framework, as shown in Fig. 1(a). CEL method can deal with the deformation and fragmentation of fluid phase during the impact process, but the introduction of additional fixed Euler calculation domain led to very low the calculation efficiency low[4–6]. In the pure FEM method, the fluid medium, the abrasive particles, and the solid phase were all described by FEM grid, as shown in Fig. 1(b). Ma et al.[7] used pure FEM method to study the erosion behavior of the high-speed water-jet. Due to the grid distortion during the impact process, the numerical accuracy and stability were affected, and the calculation was even suspended. Junkar

College of Mechanical and Electrical Engineering, Qingdao University, 308 Ningxia Rd, Qingdao, China. ✉email: hguannan@qdu.edu.cn

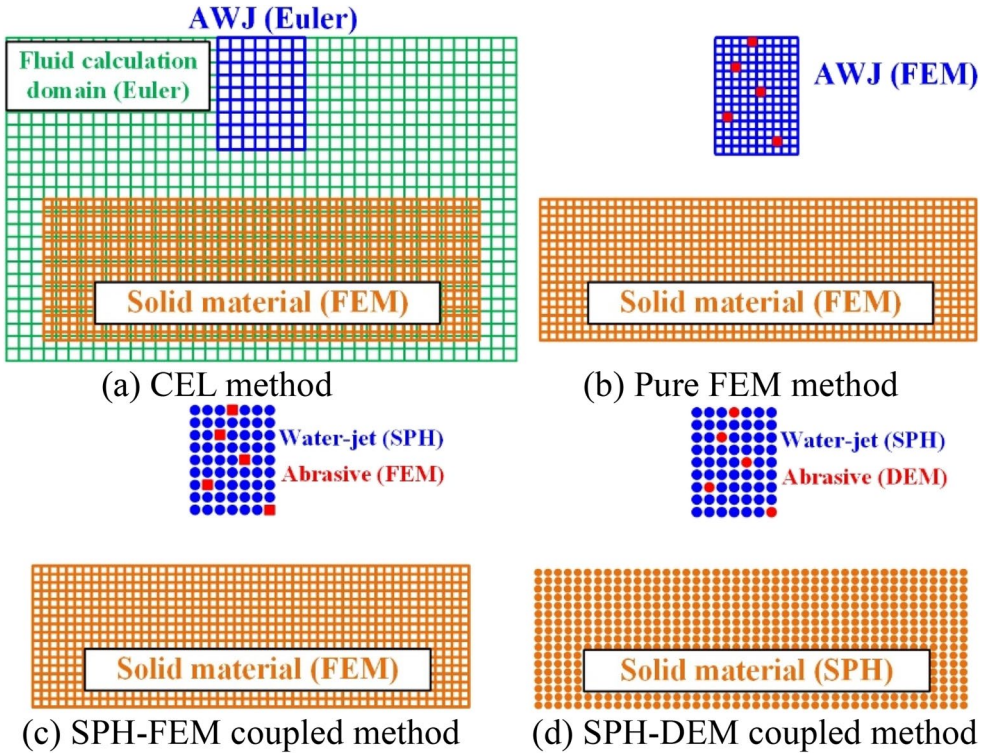


**Figure 1**. Numerical models for AWJ simulation. (**a**) CEL method (Applied in Ref.[4–6]) (**b**) Pure FEM method (Applied in Ref[7,8]). (**c**) SPH-FEM coupled method (Applied in Ref.[9–16]) (**d**) SPH-DEM coupled method (Applied in present study).

et al.[8] adopted pure FEM method to model the abrasive particles and solid materials and studied the material removal process was studied by AWJ impact, but the influence of fluid medium was ignored.

At present, SPH-FEM coupled method is widely used in AWJ simulation, as shown in Fig. 1(c). The fluid medium is modelled by SPH method, while the abrasive particles and the solid materials are described by FEM method. As a meshfree Lagrange method, SPH has been used in particle impact study. During the simulation, the continuous medium (fluid and solid material) is discretized into a series of regularly arranged SPH particles, replacing the nodes and grid elements in FEM method. These particles have their own field variables and material properties, and move according to their own velocity and acceleration. The SPH method has more advantages than FEM when dealing with large displacement and deformation problems, such as single-particle impact[17], multi-particle impact[18] and particle embedding in the targeted material[19]. Wang et al.[9] proposed a SPH-FEM model to predict the AWJ cutting performance on ductile materials within the working pressure range of 100 ~ 350 MPa. Liu et al.[10,11] investigated the influence of nozzle position on rock-breaking of the cutter with water-jet assistance. Results showed that the effect of the rear water-jet was better than the front water-jet, and the optimal incident angle was 10°. Jiang et al.[12,13] used SPH-FEM coupled method to study the crack initiation and expansion mechanism inside the rocks by water-jet impact, and concluded that the rock-breaking volume of pulsed water-jet was higher than that of continuous water-jet in the same condition of energy loss. Ren et al.[14–16] investigated the rock failure mechanism by particle water-jet impact based on SPH-FEM method. Results showed that the rock failure occurred instantaneously (within microseconds), presenting a cyclic process of "damage-cumulative damage-failure-cumulative damage-failure". The optimal jet incident velocity and particle volume fraction were also obtained.

In above researches, due to the limitations of grid-based methods, the numerical accuracy and stability of FEM heavily depend on the quantity and quality of grid. When dealing with large deformation and crack propagation problems, only the methods of mesh deletion or mesh repartition can be used to overcome highly distorted elements. For the mesh deletion method, it is difficult to reproduce the chip separation phenomenon of solid material by particle impact. While the grid repartition method needs to remesh the solid material at each time step, the computational efficiency can be greatly reduced. Coupling with the Discrete Element Method (DEM) may be an effective approach. According to solving modes of fluid-abrasive interaction, the coupling of SPH and DEM methods can be mainly categorized into two groups: the fully resolved and unresolved methods. In the fully resolved methods, each abrasive particle is arranged by a group of DEM particles, which serve as the boundaries for the abrasive particle in the fluid phase. Peng et al.[20] studied the suspension flows containing solid particles, indicating that the fully resolved SPH-DEM coupling model can reproduce the interaction between non-Newtonian fluid flows and fixed/moving solid particles with complex irregular shapes. Joubert et al.[21] proposed a fully resolved model with SPH gradient correction measures to investigate the drag characteristics of several particle shapes and topologies in the fluid phase. Results showed that the model can solve various

fluid behaviors related to the geometry of solid particles even at low resolutions. Hashemi et al.[22] investigated the movement of suspended solid bodies in Oldroyd-B fluid flows by using a modified boundary treatment technique, which could fully resolve the interaction between the fluid phase and the solid particles. Shi et al.[23] established a soil–water SPH coupling model to simulate the landslide process, and the generated wave of the landslide body could be resolved satisfactorily.

Since the fluid-solid interaction takes into account the real particle shape and spacing, the fully resolved method is particularly useful when the phenomena is concentrated on the behavior of a single solid particle or flow disturbances of a few particles. However, when simulating the fluid-particle flow contains a large number of solid particles, or the research scale is much larger than the particle diameter, the computational load to fully resolve the fluid-particle interaction may be extremely high. In these applications, the unresolved coupling method can be an effective alternative, in which the local averaged governing equations are solved based on the local porosity, and the interactions between phases are considered through semi-theoretical correlations or empirical force correlations. Robinson et al.[24] used an unresolved SPH-DEM coupling method to simulate the single/multiple particle sedimentation of fluid–particle flow, which was suitable for both dilute and dense particle flow problems. Jo et al.[25] conducted a gas–liquid–solid analysis on the packed bed flow, indicating that the local averaged techniques could accurately achieve the momentum exchange between three phases. Wu et al.[26] investigated the single/multiple particle sedimentation and dam-break processes based on the unresolved SPH-DEM coupling model, which can handle the solid structural fractures caused by fluid impact. Sun et al.[27] performed three-dimensional simulations of a quasi-steady flow in a rotating cylindrical tank, proving the unresolved model was suitable for simulating fluid-particle flow.

The unresolved coupling method has been widely used in fluid-particle interaction study such as debris flow simulation, but rarely involves the AWJ impact process. In this study, an unresolved SPH-DEM model is proposed to investigate the AWJ erosion performance on ductile and brittle materials based on our previous research[28], as shown in Fig. 1(d). The fluid and solid phases are described by SPH method, and the abrasives are described by DEM method. The unresolved coupling between SPH and DEM particles is carried out by the local averaging technique in fluid and abrasive phases, and the calculations are conducted by introducing empirical formulas for hydrodynamic and drag force estimation. The model enables the detailed interactions between water-jet, abrasives and solid materials.

The paper is organized as follows: in Sect. 2, the basic theories of SPH and DEM methods are introduced respectively. In Sect. 3, the unresolved coupling between SPH and DEM particles is involved. In Sect. 4, the proposed model is verified by comparing with the impact experiment, and the erosion process of AWJ impact on ductile and brittle materials is compared and discussed. Finally, the conclusions are summarized in Sect. 5.

## Description of DEM and SPH methods

In this study, the fluid and solid phases are discretized with SPH particles, while each abrasive particle is modelled by a single DEM particle. The interactions among these three phases are shown in Fig. 2. For the 2D model, the abrasive particles are treated as circular rigid bodies, which can be described by rigid motion equations. The motion of fluid and solid phases is described by N-S equations. In the unresolved SPH-DEM coupled method, the coupling force $\vec{F}_{af}$ between abrasive (DEM particle) and fluid (SPH particle) phases is calculated by local averaging techniques. The interaction force $\vec{F}_{fs}$ between fluid and solid phases is solved by SPH integration, while the force $\vec{F}_{as}$ between abrasive and solid phases is solved by contact algorithm. The interaction forces mentioned above will be discussed in following paragraphs.

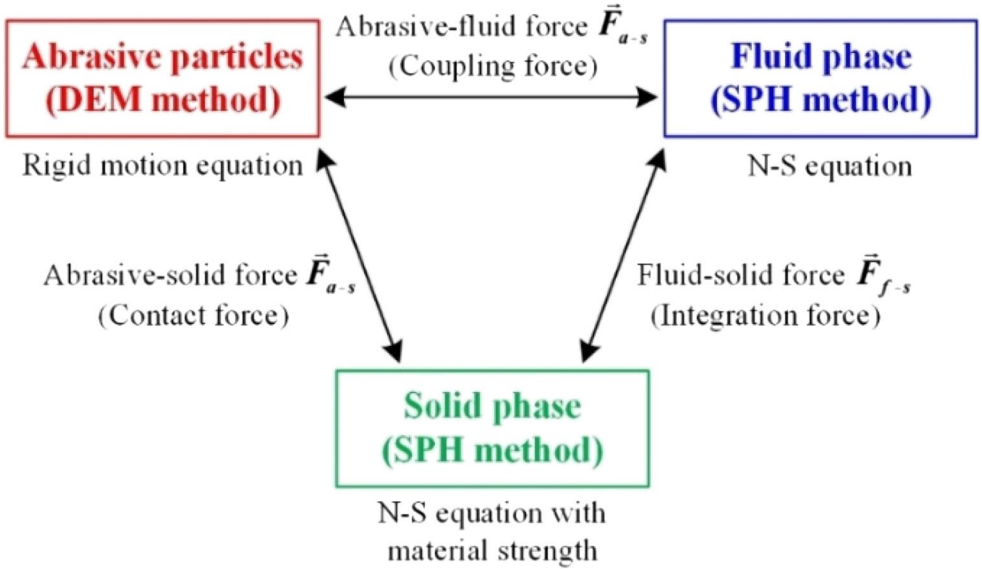


**Figure 2**. Interactions among the phases during AWJ impact.

## DEM motion equations

For rigid bodies, Newton's second law can be used to describe the motion of abrasive DEM particles, as shown below:

$$\begin{cases} m_i \frac{d\vec{v}_i}{dt} = \vec{F}_{a-a} + \vec{F}_{a-s} + \vec{F}_{a-f} + m_i \vec{g} \\ I_i \frac{d\vec{\omega}_i}{dt} = \vec{T}_{a-a} + \vec{T}_{a-s} \end{cases}, \tag{1}$$

where $m_i$, $I_i$, $\vec{v}_i$ and $\vec{\omega}_i$ are the mass, inertia, centroid velocity and angular velocity of the DEM particle $i$, respectively. $\vec{T}_{aa}$ and $\vec{T}_{as}$ are the total contact torques for abrasive-abrasive and abrasive-solid interaction, respectively. For ease of reading, the subscripts $i$ and $j$ represent abrasive DEM particles, while the subscripts $a$ and $b$ are labeled as SPH particles.

## DEM contact modelling between abrasive particles

DEM method was first proposed by Cundall and Strack to investigate the discontinuous mechanical effects inside the rocks[29]. The continuous rock medium was discretized into a series of circular (2D) and spherical (3D) DEM particles. The method was widely used in the study of geotechnical engineering and geological hazards to track the movement of solid particles inside the fluid phase[30]. In DEM calculation process, the size and shape of each particle remains unchanged, and the contact force is generated by squeezing and overlapping. Considering the energy conversion and loss during the interaction, the soft-sphere contact model can be used to handle the contact force between DEM particles[31], as shown in Fig. 3. The contact force $\vec{F}^c_{ij}$ between DEM particle $i$ and $j$ is composed by a spring, a damper and a slider, which can be divided into normal contact force $\vec{F}^n_{ij}$ and tangential contact force $\vec{F}^t_{ij}$, expressed as:

$$\begin{cases} \vec{F}^n_{ij} = -k_n \delta_n \vec{n} - d_n \vec{v}^n_{ij} \\ \vec{F}^t_{ij} = -k_t \delta_t \vec{t} - d_t \vec{v}^t_{ij} \end{cases}, \tag{2}$$

where the superscripts $n$ and $t$ represent the normal and tangential directions, respectively. $\vec{n}$ and $\vec{t}$ are the unit normal and unit tangent vectors, respectively. $k$ and $\eta$ are the stiffness and damping coefficients, respectively. $\delta$ and $\vec{v}_{ij}$ denote the overlap and relative velocity between DEM particle $i$ and $j$, respectively.

In addition, the tangential contact force $\vec{F}^t_{ij}$ is limited by the sliding condition. When $\vec{F}^t_{ij}$ is greater than the sliding friction force, the two particles will slide relative to each other, and the expression of $\vec{F}^t_{ij}$ in Eq. (2) can be rewritten as:

$$\begin{cases} \vec{F}^t_{ij} = -k_t \delta_t \vec{t} - d_t \vec{v}^t_{ij} & \left|\vec{F}^t_{ij}\right| \leqslant \mu \left|\vec{F}^n_{ij}\right| \\ \vec{F}^t_{ij} = -\mu \left|\vec{F}^n_{ij}\right| \vec{t} & \left|\vec{F}^t_{ij}\right| > \mu \left|\vec{F}^n_{ij}\right| \end{cases}, \tag{3}$$

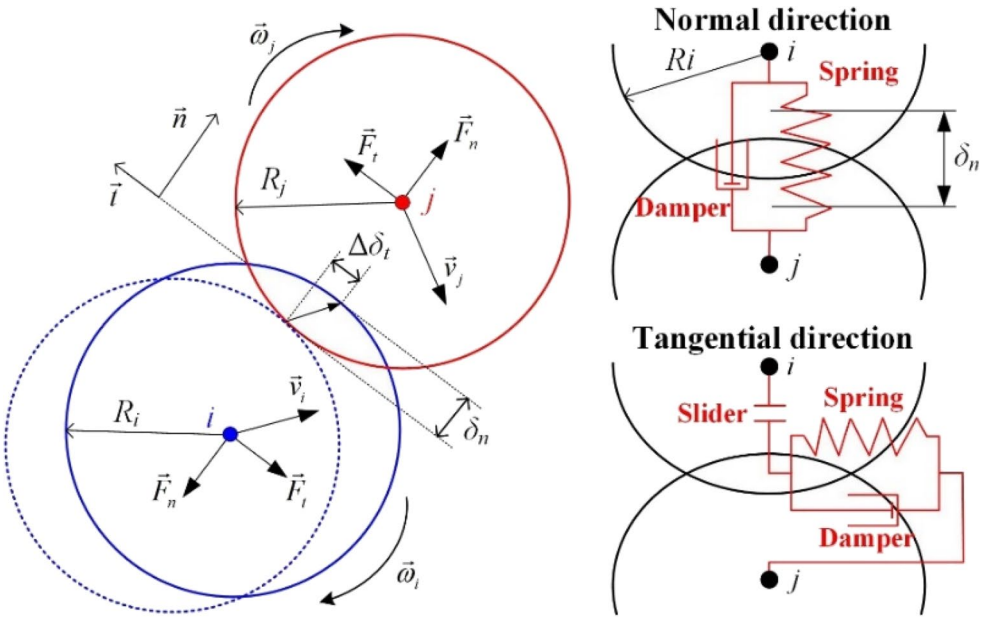


**Figure 3**. Soft-sphere contact model for DEM particles.

where $\mu$ is the sliding friction coefficient.

In summary, for abrasive-abrasive interaction, the total contact force $\vec{F}_{aa}$ and total contact torque $\vec{T}_{aa}$ of DEM particle $i$ can be calculated as:

$$\begin{cases} \vec{F}_{a-a} = \sum_j (\vec{F}_{ij}^n + \vec{F}_{ij}^t) \\ \vec{T}_{a-a} = \sum_j (\vec{F}_{ij}^t \times R_i \vec{n}) \end{cases}, \tag{4}$$

where $j$ represents all DEM particles in contact with particle $i$, and $R_i$ is the radius of the particle $i$.

*Determination of overlap δ and relative velocity* $\vec{v}_{ij}$

As shown in Fig. 3, the dotted circle indicates the position of DEM particle $i$ during the previous time step. With the relative motion of $i$ and $j$, the two particles overlap and generate the contact force. The normal overlap $\delta_n$ is given by:

$$\delta_n = R_i + R_j - |\vec{x}_{ij}|, \tag{5}$$

where $|\vec{x}_{ij}| = |\vec{x}_i - \vec{x}_j|$ is the distance between particle $i$ and $j$.

The direction of the unit normal vector $\vec{n}$ points from $i$ to $j$, expressed as:

$$\vec{n} = \frac{\vec{x}_j - \vec{x}_i}{|\vec{x}_j - \vec{x}_i|}. \tag{6}$$

The relative velocity $\vec{v}_{ij}$ depends on the position vector, the centroid velocity, and the angular velocity of the two particles, which is calculated follows:

$$\begin{cases} \vec{v}_{ij} = \vec{v}_i - \vec{v}_j + (R_i\vec{\omega}_i + R_j\vec{\omega}_j) \times \vec{n} \\ \vec{v}_{ij}^n = (\vec{v}_{ij} \cdot \vec{n})\, \vec{n} \\ \vec{v}_{ij}^t = \vec{v}_{ij} - \vec{v}_{ij}^n \end{cases}. \tag{7}$$

Therefore, the unit tangent vector $\vec{t}$ of DEM particle $i$ can be determined as:

$$\vec{t} = \frac{\vec{v}_{ij}^t}{|\vec{v}_{ij}^t|}. \tag{8}$$

Different from the normal overlap $\delta_n$, the tangential overlap $\delta_t$ is an integral variable, obtained by the accumulation of the tangential overlap increment $\Delta\delta_t$ in each time step, and can be expressed as:

$$\delta_t = \delta_t' + \Delta\delta_t = \delta_t' + \vec{v}_{ij}^t \cdot \Delta t, \tag{9}$$

where $\Delta\delta_t'$ is the tangential overlap of the previous time step, and $\delta_t' = 0$ when the contact does not exist. So $\delta_t'$ obtained in each time step needs to be saved as the basis for the calculation in the next integration period.

*Determination of stiffness coefficient k and damping coefficient d*

According to Hertz contact theory, the normal stiffness coefficient $k_n$ and the tangential stiffness coefficient $k_t$ are related to the size, elastic modulus and Poisson's ratio of DEM particles. In the case of ignoring particle deformation, $k_n$ and $k_t$ can be treated as constants, shown as below[32]:

$$\begin{cases} k_n = \frac{2E_iR_iE_jR_j}{E_iR_i+E_jR_j} \\ k_t = \frac{2E_iR_i\nu_iE_jR_j\nu_j}{E_iR_i\nu_i+E_jR_j\nu_j} \end{cases}, \tag{10}$$

where $E$, $\nu$, $G$ and $R$ are the elastic modulus, Poisson's ratio, shear modulus and radius of the DEM particle, respectively.

In the soft-sphere contact model, the collision of DEM particles can be regarded as the movement of spring vibrator. For a spring oscillator with mass $m$, the normal damping coefficient $d_n$ and tangential damping coefficient $d_t$ depend on the stiffness coefficients, which can be expressed as[33]:

$$\begin{cases} d_n = 2\xi\sqrt{mk_n} \\ d_t = 2\xi\sqrt{mk_t} \end{cases}, \tag{11}$$

where $\xi = -\ln e/\sqrt{\pi^2 + \ln^2 e}$ is the damping ratio, and $e$ is the restitution coefficient, which needs to be measured by experiment.

When $e = 1.0$, $\xi = d_n = d_t = 0$, the contact between DEM particles are completely elastic without any damping effect. Therefore, there is no energy loss during the conversion process of mechanical energy and elastic potential energy. When $e \approx 0$, $\xi \approx 1$, the particles are in the critical damping conditions, and the kinetic energy is damped at the maximum speed. The effect of restitution coefficient $e$ on DEM particle collisions is shown in Fig. 4. In the

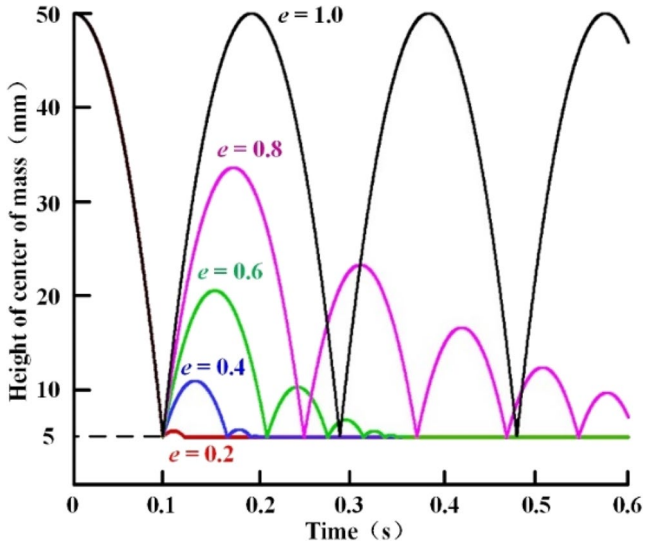


**Figure 4**. Effect of recovery coefficient *e* on DEM particle collisions.

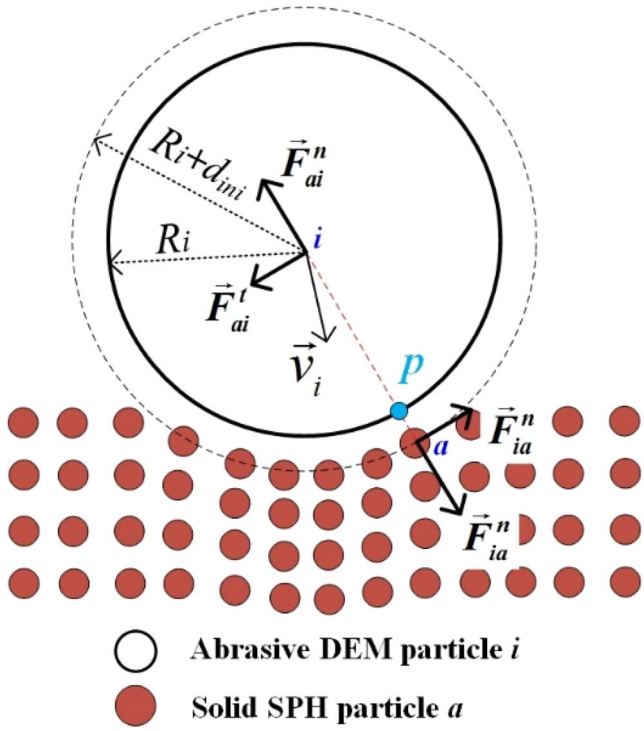


**Figure 5**. Contact force between abrasive and solid phases.

simulation, a single DEM particle has a radius of 5 mm and an initial height of 50 mm, falling freely at $t = 0$, and makes contact with the bottom boundary at about $t = 0.096$s. As shown in Fig. 4, when $e = 1.0$, the particle can rebound to the initial height and cycle repeatedly, which means that the particle mechanical energy is conserved during the collisions. With the decrease of *e*, the height of the particle rebound decreases, and the damping coefficient increases gradually, leading to the attenuation effect on the kinetic energy. Finally the mechanical energy is exhausted, making the particle stop at the bottom boundary.

## DEM contact modelling between abrasive and solid phases

The contact illustration between abrasive and solid phases is shown in Fig. 5. The abrasive particle is circular (2D) and consists of a DEM particle with a well-defined boundary, which is treated as a rigid body during the collision. The contact type between solid SPH particles and rigid abrasive DEM particles belongs to point-line contact. The solid particles move relative to each other under the action of rigid boundary, resulting in

deformation and surface damage. Therefore, the penalty function algorithm is adopted to calculate the contact force according to the overlap between the solid SPH particle and the rigid DEM boundary, which can be divided into the following 4 steps[34]:

(1) Contact detection: when the solid SPH particle $a$ ($x_a$, $y_a$) is close enough to the boundary of the rigid DEM particle (inside the dotted circle in Fig. 5), the contact is detected.
(2) Determination of contact point $p$: contact point $p$ is located on the boundary of DEM particle $i$, and also on the line between DEM particle $i$ and SPH particle $a$, as shown in Fig. 5.
(3) Determination of unit normal vector $\vec{n}_p$ and unit tangent vector $\vec{t}_p$: the unit normal vector direction $\vec{n}_p$ points from $i$ to $a$. The unit tangent vector $\vec{t}_p$ is determined by the tangential component of relative velocity $\vec{v}_{pa}$, as follows:

$$\begin{cases} \vec{v}_{pa} = \vec{v}_p - \vec{v}_a \\ \vec{v}_p = \vec{v}_i + \vec{\omega}_i \times (\vec{x}_p - \vec{x}_i) \end{cases}, \tag{12}$$

where $\vec{v}_p$ is the velocity on point $p$. $\vec{x}_i$ is the position vector of DEM particle $i$.

(4) Determination of overlap $d_n$ and contact force $\vec{F}_{ia}$: the distance $d_p$ between the solid SPH particle $a$ and the contact point $p$ is obtained at first. If $d_p < d_{ini}$ ($d_{ini}$ is the initial spacing of SPH particles), the overlap is determined by $d_n = d_{ini} - d_p$. The contact force $\vec{F}_{ia}$ can be divided into the normal contact force $\vec{F}^n_{ia}$ and the tangential contact force $\vec{F}^t_{ia}$, which can be written as:

$$\begin{cases} \vec{F}^n_{ia} = (1-\chi)\left[\frac{2m_a}{(\Delta t)^2} d_n\right]\vec{n} \\ \vec{F}^t_{ia} = \min\left(\frac{2m_a}{\Delta t}\left(\vec{v}_{pa}\cdot\vec{t}_p\right)\vec{t}_p, \mu\left|\vec{F}^n_{ia}\right|\vec{t}_p\right) \end{cases}, \tag{13}$$

where $\chi$ is the overlap coefficient ($\chi = 0$ means no overlap is allowed). $m_a$ is the mass of SPH particle $a$, and $\Delta t$ is the length of a single time step. Tangential contact force $\vec{F}^t_{ia}$ is limited by the sliding friction force $\mu\left|\vec{F}^n_{ia}\right|$.

According to Newton's third law, the contact force $\vec{F}_{ai}$ of abrasive DEM particle $i$ is applied in the opposite direction to $\vec{F}_{ia}$, and the force functional point is contact point $p$. Therefore, the total contact force $\vec{F}_{as}$ and the total contact force $\vec{T}_{as}$ for abrasive-solid interaction can be obtained by:

$$\begin{cases} \vec{F}_{a-s} = \sum_a \vec{F}_{ai} \\ \vec{T}_{a-s} = \sum_a \left[\vec{F}_{ai} \times (\vec{x}_p - \vec{x}_i)\right] \end{cases}, \tag{14}$$

where $a$ represents all solid SPH particles in contact with DEM particle $i$.

## SPH modelling for fluid phase based on local average technique

Unlike the grid-based numerical methods, SPH method uses a finite number of particles to represent the continuous medium. The SPH particles have their own field variables and material properties, such as velocity, mass, density, stress, etc[35]. The motion equations for SPH particles are based on the continuum mechanics conservation laws, and the particle properties change over time due to the interactions with other neighboring particles within the support domain[36]. These characteristics make SPH method suitable for large impact and deformation problems. The advantages of SPH method lie in the conceptual simplicity, straightforward implementation, and easy introduction of new physical quantities[37].

Two key steps are needed for SPH formulation: integral representation (kernel approximation) and particle approximation. By the process of these two steps, the field function $f(\vec{x})$ and the special derivative $\nabla f(\vec{x})$ of SPH particle $a$ can be approximated as:

$$\langle f(\vec{x}_a)\rangle = \sum_{b=1}^{N} \frac{m_b}{\rho_b} f(\vec{x}_b)\cdot W(\vec{x}_a - \vec{x}_b, h), \tag{15}$$

$$\left\langle \frac{\partial f(\vec{x}_a)}{\partial \vec{x}} \right\rangle = \sum_{b=1}^{N} \frac{m_b}{\rho_b} f(\vec{x}_b)\cdot \frac{\partial W_{ab}}{\partial \vec{x}_a}, \tag{16}$$

where $\vec{x}_a$ is the position vector of SPH particle $a$. Subscript $b$ means the neighboring particles in the support domain of particle $a$. $m$ and $\rho$ are the mass and material density of the SPH particle, respectively. $N$ is the total number of the neighboring particles. $\frac{\partial W_{ab}}{\partial \vec{x}_a}$ is the kernel gradient, which can be written as $\frac{\partial W_{ab}}{\partial \vec{x}_a} = \frac{\vec{x}_a - \vec{x}_b}{r_{ab}}\frac{\partial W_{ab}}{\partial r_{ab}} = \frac{\vec{x}_{ab}}{r_{ab}}\frac{\partial W_{ab}}{\partial r_{ab}}$, and $r_{ab}$ is the distance between particle $a$ and $b$.

In Eq. (15), $W(\vec{x}_a - \vec{x}_b, h)$ is the smoothing function for SPH formulation, and $h$ is the smoothing length. There are many possible choices of the smoothing function, and the cubic spline function is selected in this study, expressed as[38]:

$$W(\vec{x}_a - \vec{x}_b, h) = W_{ab} = a_d \times \begin{cases} \frac{2}{3} - q^2 + \frac{1}{2}q^3, \ 0 \leqslant q < 1 \\ \frac{1}{6}(2-q)^3, \ 1 \leqslant q < 2 \\ 0, \ q \geqslant 2 \end{cases}, \tag{17}$$

where $a_d$ is the normalization factor with $a_d = 15/(7\pi h^2)$ for the two-dimensional problem. $q = r_{ab}/h$ is the normalization distance between particle $a$ and $b$. When $q \geq 2$, $W_{ab} = 0$, which indicates that the radius of the support domain is $2h$. The selection of $h$ value is very important for the calculation accuracy and efficiency. In this study, $h = 1.25d_{ini}$, which is the most widely used in SPH formulation.

*Local average variables in SPH*

When the fluid medium contains a large number of abrasive particles, it requires a lot of computation to solve the N-S equation and Newton's equation directly by using the fully-resolved coupled method. In this case, the unresolved SPH-DEM coupled method may be a better choice for modeling the abrasive-fluid interaction. The local average technique is adopted to solve the coupling force between fluid phase (SPH) and abrasive particles (DEM). The concept was first proposed by Anderson and Jackson[39] to deal with the momentum transitions between different phases in suspension by defining local average variables on fluid and particle phases instead of some field variables (such as fluid density, fluid velocity, and particle velocity, etc.). These local average variables at any point $x$ in the fluid domain can be obtained by convolution with the smoothing function, as shown below:

$$\langle \bar{f}(x) \rangle = \epsilon(x) f(x) = \int_{\text{fluid}} \bar{f}(x') W(x - x') dV, \tag{18}$$

$$\epsilon(x) = 1 - \int_{\text{particle}} W(x - x') dV, \tag{19}$$

where $\bar{f}(x)$ is the local average value of the field function $f(x)$. $\epsilon(x)$ is the local porosity at point $x$, which depends on the number and distance of neighboring DEM particles. If there are no DEM particles nearby, $\epsilon(x) = 1$.

By the particle approximation process in Eq. (19), the local porosity of SPH particle $a$ can be expressed as[40]:

$$\epsilon \ominus_a = 1 - \sum_j W_{aj}(h_c) \ V_j, \tag{20}$$

where $V_j$ is the volume of DEM particle $j$ near SPH particle $a$, and $h_c$ is the coupling smoothing length.

Therefore, the locally averaged density $\bar{\rho}_a$ of the fluid SPH particle $a$ is written as:

$$\overline{\rho}_a = \varepsilon_a \rho_a, \tag{21}$$

where $\rho_a$ is the actual density of SPH particle $a$.

*SPH motion equations for fluid phase*

The motion equations for fluid phase are based on the N-S equations, and the continuity and momentum equations in SPH formulation based on the local average technique are given by:

$$\frac{\mathrm{d}\overline{\rho}_a}{\mathrm{d}t} = \overline{\rho}_a \sum_{b=1}^{N} \frac{m_b}{\overline{\rho}_b} (\vec{v}_a^{\alpha} - \vec{v}_b^{\alpha}) \cdot \frac{\partial W_{ab}}{\partial \vec{x}_a^{\alpha}}, \tag{22}$$

$$\frac{\mathrm{d}\vec{v}_a^{\alpha}}{\mathrm{d}t} = \sum_{b=1}^{N} m_b \left[ -\left( \frac{P_a}{\overline{\rho}_a^2} + \frac{P_b}{\overline{\rho}_b^2} \right) + \Pi_{ab}^{visc} - \pi_{ab}^{art} \right] \cdot \frac{\partial W_{ab}}{\partial \vec{x}_a^{\alpha}} + \vec{F}_{f-a}^{\alpha} + \vec{F}_{f-s}^{\alpha} + \vec{g}^{\alpha}, \tag{23}$$

where $\vec{v}_a$ and $P_a$ are the velocity and pressure of SPH particle $a$, respectively. $\vec{F}_{f-a}$ and $\vec{F}_{f-s}$ are the abrasive-fluid coupling force and the solid-fluid contact force, respectively.

In Eq. (23), the first term is the pressure term, which is determined by the equation of state (EOS). For the fluid phase, the Mie-Gruneisen EOS equation is adopted to describe the pressure wave effect of the fluid medium during the impact, which can be expressed as[41]:

$$P = \frac{\rho_0 c_0^2 \eta \left[ 1 + \left( 1 - \frac{\Gamma_0}{2} \right) \eta - \frac{a}{2} \eta^2 \right]}{\left[ 1 - (S_1 - 1)\eta - S_2 \frac{\eta^2}{\eta + 1} - S_3 \frac{\eta^2}{(\eta+1)^2} \right]^2} + (\Gamma_0 + a\eta) e, \tag{24}$$

where $\eta = \bar{\rho}/\rho_0 - 1$, and $\rho_0$ is the reference density. $e$ is the internal energy per unit of mass. The EOS parameters of the fluid phase are listed in Table 1.

The second term $\prod_{ab}^{visc}$ in Eq. (23) is the physical viscous force term, which is used to calculate the viscous force in Newtonian fluids and can be expressed as[43]:

| Parameters | Value |
|---|---|
| Reference density | $\rho_0 = 1000$ kg/m$^3$ |
| Velocity of sound | $c_0 = 1480$ m/s |
| Grüneisen gamma | $\Gamma_0 = 0.5$ |
| Volume correction coefficient | $A = 0$ |
| Coefficient | $S_1 = 2.56$ |
| Coefficient | $S_2 = 1.98$ |
| Coefficient | $S_3 = 1.23$ |

**Table 1**. EOS parameters for fluid phase[42].

$$\Pi_{ab}^{visc} = \sum_{b=1}^{N} m_b \left[ \frac{4\mu_f \vec{r}_{ab}}{(\bar{\rho}_a + \bar{\rho}_b)|\vec{r}_{ab}|^2} \right] \cdot \vec{v}_{ab} \tag{25}$$

where $\mu_f$ is the fluid kinematic viscosity.

The third term $\pi_{ab}^{art}$ is the artificial viscosity term, which is proposed by Monaghan[44] to suppress the unphysical pressure oscillations in the simulation, as shown below:

$$\boldsymbol{\pi}_{ab}^{art} = \begin{cases} \frac{-\alpha_{\boldsymbol{\pi}} \bar{c}_{ab} \phi_{ab} + \beta_{\boldsymbol{\pi}} \phi_{ab}{}^2}{\bar{\rho}_{ab}}, \vec{v}_{ij} \cdot \vec{x}_{ij} < 0 \\ 0, \vec{v}_{ij} \cdot \vec{x}_{ij} \geqslant 0 \end{cases}, \tag{26}$$

where $c_a$ is the sound speed of SPH particle $a$, $\bar{c}_{ab} = (c_a + c_b)/2$. $\bar{\rho}_{ab} = (\bar{\rho}_a + \bar{\rho}_b)/2$. The coefficient $\phi_{ab}$ is expressed as:

$$\phi_{ab} = \frac{\bar{h}_{ab} (\vec{v}_{ab} \cdot \vec{x}_{ab})}{|\vec{x}_{ab}|^2 + (0.1\bar{h}_{ab})^2}, \tag{27}$$

where $\bar{h}_{ab} = (h_a + h_b)/2$, $\vec{v}_{ab} = \vec{v}_a - \vec{v}_b$ and $\vec{x}_{ab} = \vec{x}_a - \vec{x}_b$.

$\alpha_\pi$ and $\beta_\pi$ in Eq. (26) are the energy dissipation coefficients, which are determined by medium characteristics. $\alpha_\pi$ is related to the volumetric viscosity, while $\beta_\pi$ is applied to prevent the penetration between SPH particles during high-speed impacts. Monaghan chose $\alpha_\pi = \beta_\pi = 0.01$ when dealing with the free surface flow problems, and suggested that values of $\alpha_\pi$ and $\beta_\pi$ can be around 1.0 in most cases[45]. Randles et al. chose $\alpha_\pi = \beta_\pi = 2.5$ when studying the high-speed impact (~ 1 km/s) of metal materials such as copper and steel[46]. The total system energy is not conserved due to the dissipation of the particles' kinetic energy with artificial viscosity term. Therefore, on the premise of eliminating non-physical oscillations, the energy dissipation coefficients should be selected as small as possible to ensure the numerical stability. In this study, $\alpha_\pi = \beta_\pi = 0.1$ is used for the fluid phase and $\alpha_\pi = \beta_\pi = 1.0$ for the solid phase.

## SPH modelling for solid phase

Similar to the fluid phase, the motion equations for the solid SPH particles are shown as follows:

$$\frac{d\rho_a}{dt} = \rho_a \sum_{b=1}^{N} \frac{m_b}{\rho_b} \vec{v}_{ab}^{\alpha} \cdot \frac{\partial W_{ab}}{\partial \vec{x}_a^{\alpha}}, \tag{28}$$

$$\frac{d\vec{v}_a^{\alpha}}{dt} = \sum_{b=1}^{N} m_b \left[ -\left( \frac{P_a}{\rho_a^2} + \frac{P_b}{\rho_b^2} \right) - \pi_{ab}^{art} \right] \frac{\partial W_{ab}}{\partial \vec{x}_a^{\alpha}} + \sum_{b=1}^{N} m_b \left( \frac{\vec{\tau}_a^{\alpha\beta}}{\rho_a^2} + \frac{\vec{\tau}_b^{\alpha\beta}}{\rho_b^2} \right) \frac{\partial W_{ab}}{\partial \vec{x}_a^{\beta}} + \vec{F}_{a-s}^{\alpha} + \vec{F}_{f-s}^{\alpha} + \vec{g}^{\alpha}, \tag{29}$$

where the second term in Eq. (29) is the shear stress term, and $\vec{\tau}_a$ is the deviatoric stress tensor.

According to the solid mechanics, $\vec{\tau}_a$ is determined by the deviator stress rate $\dot{\vec{\tau}}_a$. $\dot{\vec{\tau}}_a$ is proportional to the strain rate $\dot{\vec{\varepsilon}}$, and the proportional coefficient is the shear modulus $G$. For explicit dynamic simulation, the deviator stress rate is obtained by Hook's law with the Jaumann rate correction, expressed as[35]:

$$\dot{\vec{\tau}}_a = \frac{d\vec{\tau}_a^{\alpha\beta}}{dt} = 2G(\dot{\vec{\varepsilon}}_a^{\alpha\beta} - \frac{1}{3}\delta^{\alpha\beta}\dot{\vec{\varepsilon}}_a^{\gamma\gamma}) + \vec{\tau}_a^{\alpha\gamma} \cdot \dot{\vec{R}}_a^{\beta\gamma} + \vec{\tau}_a^{\gamma\beta} \cdot \dot{\vec{R}}_a^{\alpha\gamma}, \tag{30}$$

where $\dot{\vec{\varepsilon}}_a$ and $\dot{\vec{R}}_a^{\beta\gamma}$ are the strain rate tensor and rotation rate tensor, respectively, as shown in follows[47]:

$$\begin{cases} \dot{\vec{\varepsilon}}_a^{\alpha\beta} = \frac{1}{2}\sum_{b=1}^{N}\left(\frac{m_b}{\rho_b}\vec{v}_{ba}^{\alpha}\cdot\frac{\partial W_{ab}}{\partial \vec{x}_a^{\beta}} + \frac{m_b}{\rho_b}\vec{v}_{ba}^{\beta}\cdot\frac{\partial W_{ab}}{\partial \vec{x}_a^{\alpha}}\right) \\ \dot{\vec{R}}_a^{\alpha\beta} = \frac{1}{2}\sum_{b=1}^{N}\left(\frac{m_b}{\rho_b}\vec{v}_{ba}^{\alpha}\cdot\frac{\partial W_{ab}}{\partial \vec{x}_a^{\beta}} - \frac{m_b}{\rho_b}\vec{v}_{ba}^{\beta}\cdot\frac{\partial W_{ab}}{\partial \vec{x}_a^{\alpha}}\right) \end{cases}. \tag{31}$$

The deviatoric stress tensor $\vec{\tau}_a$ can be obtained by integrating Eq. (30) with time, and the integration is carried out when the material is in the elastic deformation stage. If the stress exceeds the yield limit, the plastic deformation occurs. The Von-Mises yield criterion is adopted in this study. For solid SPH particle *a*, when the Von-Mises equivalent stress $\bar{\sigma}_{\mathrm{VM}} = \sqrt{\frac{3}{2}\vec{\tau}_a^{\alpha\beta}\vec{\tau}_a^{\alpha\beta}}$ exceeds the yield stress $\sigma_y$, the deviatoric stress tensor $\vec{\tau}_a$ should be brought back to the yield surface:

$$\vec{\tau}_a = \frac{\sigma_y}{\bar{\sigma}_{\mathrm{VM}}}\vec{\tau}_a. \tag{32}$$

The yield stress $\sigma_y$ can be solved by the constitutive model, which is composed of strength equation, failure equation and EOS equation. It is necessary to select a suitable constitutive model for the solid phase to study the mechanical behavior of the targeted material by AWJ impact. For ductile materials, the surface erosion process is mainly plastic deformation caused by abrasive particle impact. For brittle materials, the erosion process is mainly the surface fragmentation caused by crack diffusion.

*Ductile material*

The J-C constitutive model is selected to model the ductile materials, which is widely used to describe the strength changes of ductile materials (such steel, copper and aluminum) in high strain, high strain rate or high temperature conditions. The strength equation of J-C model is written as[48]:

$$\sigma_y = \left[A + B(\varepsilon_p)^N\right]\left[1 + C\ln\left(\frac{\dot{\varepsilon}_p}{\dot{\varepsilon}_0}\right)\right]\left[1 - (T^*)^M\right], \tag{33}$$

where $\varepsilon_p = \int \dot{\varepsilon}_p dt$ is the equivalent plastic strain, and $\dot{\varepsilon}_p = \sqrt{\frac{2}{3}\dot{\vec{\varepsilon}}_a^{\alpha\beta}\dot{\vec{\varepsilon}}_a^{\alpha\beta}}$ is the equivalent plastic strain rate. $\dot{\epsilon}_0 = 1.0\mathrm{s}^{-1}$ is the reference strain rate. *A*, *B*, *C*, *N* and *M* are material dependent constants. $T^*$ is the normalized temperature given by:

$$T^* = \frac{T - T_0}{T_m - T_0}, \tag{34}$$

where $T$ is the actual temperature. $T_0$ and $T_m$ are the reference temperature and melting temperature of the ductile material, respectively.

When the plastic deformation occurs, the failure equation is used to describe the failure process of solid phase. The failure equation of J-C model is written as[48]:

$$\varepsilon_f = \left[D_1 + D_2\exp\left(D_3\left(\frac{\sigma_m}{\bar{\sigma}_{\mathrm{VM}}}\right)\right)\right]\left[1 + D_4\ln\left(\frac{\dot{\varepsilon}_p}{\dot{\varepsilon}_0}\right)\right]\left[1 + D_5T^*\right], \tag{35}$$

where $\epsilon_f$ is the failure strain, and $D_1 \sim D_2$ are the material dependent constants. $\sigma_m$ is the mean principal stress, which is equal to the isotropic pressure $P$.

The cumulative damage failure criterion is adopted to model the material removal, and the damage factor $D$ is introduced to describe the damage accumulation. For solid SPH particle *a*, when $D \geq 1.0$, the material is considered to be completely fractured. The deviator stress $\vec{\tau}_a$ is set to zero, and the particle is deleted to represent the material removal, as shown in follows:

$$D = \sum\frac{\Delta\varepsilon_p}{\varepsilon_f}, \tag{36}$$

where $\Delta\epsilon_p$ is the equivalent plastic strain increment of the current time step.

Similar to the fluid phase, the Mie-Grüneisen EOS equation is also applied for ductile materials written as[46]:

$$P = \frac{\rho_0 c_0^2\eta\left[1 + \left(1 - \frac{\Gamma_0}{2}\right)\eta\right]}{\left[1 - (S_a - 1)\eta\right]} + \rho_0\Gamma_0 e, \tag{37}$$

where $S_a$ is the linear Hugoniot slope coefficient.

The J-C model parameters of two common ductile materials are listed in Table 2.

*Brittle material*

The JH-2 constitutive model is selected to model the brittle materials, which is developed to study the stress-strain behavior of brittle materials (such as ceramics, glass and rock) in large impact and large deformation

| Parameter properties and labels | OFHC Copper[49] | Al6061-T6[18] |
|---|---|---|
| Material basic parameters | | |
| Reference density, $\rho_0$ (kg/m$^3$) | 8960 | 2800 |
| Shear modulus, $G$ (GPa) | 46.0 | 26.0 |
| Poisson ratio, $\upsilon$ | 0.34 | 0.33 |
| J-C strength parameters | | |
| Initial yield strength, $A$ (MPa) | 90 | 335 |
| Hardening coefficient, $B$ (MPa) | 292 | 85 |
| Strain coefficient, $N$ | 0.31 | 0.11 |
| Strain rate coefficient, $C$ | 0.025 | 0.012 |
| Strain rate sensitivity index, $M$ | 1.09 | 1.6 |
| Reference temperature, $T_0$ (K) | 293 | 293 |
| Melting temperature, $T_m$ (K) | 1790 | 925 |
| J-C failure parameters | | |
| Damage constant, $D_1$ | 0.54 | -0.77 |
| Damage constant, $D_2$ | 4.89 | 1.45 |
| Damage constant, $D_3$ | -3.03 | -0.47 |
| Damage constant, $D_4$ | 0.014 | 0 |
| Damage constant, $D_5$ | 1.12 | 1.6 |
| Mie-Gruneisen EOS parameters | | |
| Sound speed, $c_0$ (m/s) | 3933 | 5240 |
| Linear Hugoniot slope coefficient, $S_a$ | 1.5 | 1.4 |
| Gruneisen coefficient, $\Gamma_0$ | 1.99 | 1.97 |

**Table 2**. J-C model parameters of common ductile materials for solid phase.

conditions. Based on the JH-1 model, the JH-2 strength equation introduces the damage factor $D$ to describe the softening effect of the brittle materials during the impact process, as shown below[50]:

$$\begin{cases} \sigma_i^* = A(P^* + T^*)^N (1 + C\ln\dot{\varepsilon}^*) \;\; D = 0 \text{ (Intact)} \\ \sigma^* = \sigma_i^* - D\left(\sigma_i^* - \sigma_f^*\right) \;\; 0 < D < 1.0 \text{ (Damaged)} \\ \sigma_f^* = B(P^*)^M (1 + C\ln\dot{\varepsilon}^*) \leqslant \sigma_{f\max}^* \;\; D = 1.0 \text{ (Fracture)} \end{cases}, \tag{38}$$

where the superscript * indicates normalization processing. The normalized strengths ($\sigma^*$, $\sigma_i^*$, $\sigma_f^*$ and $\sigma_{f\max}^*$) have the general form $\sigma^* = \sigma_y/\sigma_{HEL}$, where $\sigma_{HEL}$ is the equivalent stress at Hugoniot Elastic Limit (HEL). $A$, $N$, $C$, $B$ and $M$ are material dependent constants. $P^* = P/P_{HEL}$ and $T^* = T/P_{HEL}$ are the hydrostatic pressure and the maximum tensile strength normalized by the pressure $P_{HEL}$ at HEL, respectively. $\dot{\epsilon}^* = \dot{\epsilon}^p$ is the dimensionless strain rate, and $\dot{\epsilon}_0 = 1.0\text{s}^{-1}$ is the reference strain rate.

Similar to the ductile materials, the JH-2 failure equation for the brittle materials is given by[50]:

$$D = \sum \frac{\Delta\varepsilon_p}{\varepsilon_f} = \sum \frac{\Delta\varepsilon_p}{D_1(P^* + T^*)^{D_2}}, \tag{39}$$

where $D_1$ and $D_2$ are material constants. When the brittle material is completely fractured ($D \geq 1$), the deviator stress $\overline{\tau}_a$ is constant at zero, and the equivalent plastic strain $\epsilon_p$ no longer accumulates.

The polynomial EOS equation is employed to solve the hydrostatic pressure $P$ for brittle materials, which is actually another general form of the Mie-Grüneisen equation expressed as[51]:

$$P = \begin{cases} K_1\mu + K_2\mu^2 + K_3\mu^3 + \Delta p \;\; \mu \geqslant 0 \text{ (Compression)} \\ K_1\mu \;\; \mu < 0 \text{ (Tension)} \end{cases}, \tag{40}$$

where $\mu = \rho/\rho_0$-1 is the relative volume factor. $K_1 \sim K_3$ are material constants. $\Delta P$ is the pressure increment, representing the transformation of elastic internal energy to hydrostatic potential energy, and reflecting the expansion effect of brittle materials during the damage process. It varies from $\Delta P = 0$ at $D = 0$ to $\Delta P = \Delta P_{max}$ at $D = 1.0$ given by:

$$\Delta p_{n+1} = -K_1\mu + \sqrt{(K_1\mu + \Delta p_n)^2 + 2\beta K_1 \Delta U}, \tag{41}$$

where $\beta$ is the energy conversion coefficient ($0 \leq \beta \leq 1.0$), and $\Delta U = U_{n+1}$-$U_n$ is the internal energy loss during a single time step. The JH-2 model parameters of two common brittle materials are listed in Table 3.

The radial return algorithm is adopted to solve the deviator stress term $\vec{\tau}_a$ for the solid phase. $(\vec{\tau}_a)_{n\bullet\Delta t}$ is the deviator stress of solid SPH particle *a* at the beginning of the *n*th time step. Each time step $\Delta t$ contains two small cycles, and each cycle is $\Delta t/2$. The implementation procedures of $\vec{\tau}_a$ for the solid phase is shown in Fig. 6. For ductile and brittle materials, different constitutive models are used to solve the isotropic pressure $P_a$, the yield stress $\sigma_y$, and the damage factor *D*, while the solving process for other parameters is the same.

## Unresolved coupling between SPH and DEM methods

### Coupling force for abrasive-fluid interaction based on local averaging technique

The essence of SPH-DEM coupling is to realize the interaction between the two kinds of particles. In unresolved coupled method, the coupling force $\vec{F}_{a\text{-}f}$ for abrasive-fluid interaction in Eq. (1) is shown in Fig. 7. According to the smoothing function, the coupling radius between the two phases is $R_c = 2h_c$. For DEM particle *i*, $\vec{F}_{a\text{-}f}$ is expressed as[40]:

$$\vec{F}_{a-f} = V_i(-\nabla P + \nabla \cdot \vec{\tau})_i + \vec{F}_d, \tag{42}$$

where the first term $V_i(-\nabla P+\nabla\cdot\vec{\tau}_i)$ is the average hydrodynamic force, which represents the buoyancy and shear force of the fluid phase acting on DEM particles within $R_c$, and $V_i$ is the particle volume. The second term $\vec{F}_d$ is the drag force.

The Shepard corrected SPH interpolation is employed to solve the average hydrodynamic force term, as show in follows[54]:

$$\begin{cases} V_i(-\nabla P + \nabla \cdot \vec{\tau})_i = \frac{1}{\sum_a \frac{m_a}{\rho_a} W_{ia}(h_c)} \sum_a m_a \theta_a W_{ia}(h_c) \\ \theta_a = \sum_b m_b \left[ -\left( \frac{P_a}{\bar{\rho}_a^2} + \frac{P_b}{\bar{\rho}_b^2} \right) + \Pi_{ab}^{visc} \right] \cdot \nabla_a W_{ab}(h) \end{cases}, \tag{43}$$

where the subscript *a* represents the SPH particle within the coupling radius of DEM particle *i*, and the subscript *b* represents the SPH particle within the support domain of particle *a*.

The drag force term $\vec{F}_d$ acting on DEM particle *i* is due to the repulsion of surrounding fluid SPH particles, depending on average porosity $\epsilon_i$ and relative velocity $\vec{v}_{af}$ at point *i*, expressed as:

$$\vec{F}_d = \frac{\beta}{1 - \epsilon\ominus_i} V_i \cdot \vec{v}_{af}, \tag{44}$$

where $\epsilon_i$ and $\vec{v}_{af}$ are given by:

| Parameter properties and labels | Red sandstone[52] | Granite[53] |
|---|---|---|
| Material basic parameters | | |
| Reference density, $\rho_0$ (kg/m$^3$) | 2460 | 2660 |
| Shear modulus, *G* (GPa) | 7.84 | 21.9 |
| JH-2 strength parameters | | |
| Hugoniot elastic limit, *HEL* (GPa) | 2.5 | 4.5 |
| Pressure at HEL, $P_{HEL}$ (GPa) | 1.45 | 2.93 |
| Equivalent stress at HEL, $\sigma_{HEL}$ (GPa) | 1.58 | 2.36 |
| Intact strength coefficient, *A* | 0.88 | 1.248 |
| Intact strength coefficient, *N* | 0.64 | 0.676 |
| Fractured strength coefficient, *B* | 0.293 | 0.68 |
| Fractured strength coefficient, *M* | 0.64 | 0.83 |
| Strain rate coefficient, *C* | 0.00337 | 0.0051 |
| Normalized maximum tensile strength, *T** | 0.0103 | 0.0195 |
| Normalized maximum fractured strength, $\sigma^*_{f\max}$ | 0.25 | 0.16 |
| JH-2 failure parameters | | |
| Damage coefficient, $D_1$ | 0.05 | 0.008 |
| Damage coefficient, $D_2$ | 1.5 | 0.435 |
| Polynomial EOS parameters | | |
| Bulk modulus, $K_1$(GPa) | 10.45 | 25.7 |
| Pressure coefficient, $K_2$(GPa) | 20.78 | -386 |
| Pressure coefficient, $K_3$(GPa) | 22.69 | 12,800 |
| Energy conversion coefficient, $\beta$ | 1.0 | 1.0 |

**Table 3**. JH-2 model parameters of common brittle materials for solid phase.

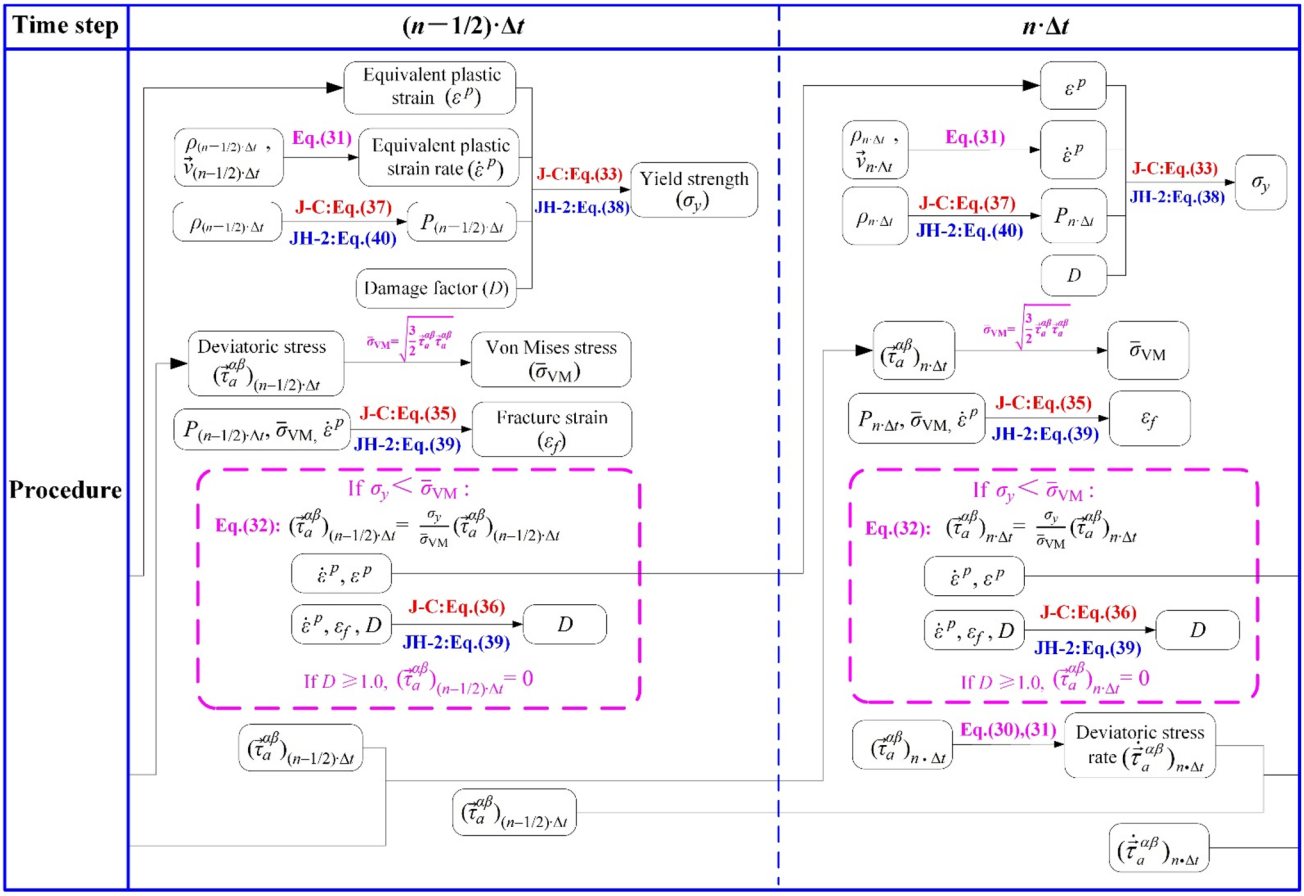


**Figure 6**. Implementation procedures of deviatoric stress term $\vec{\tau}_a$ for solid phase (In a single time step)

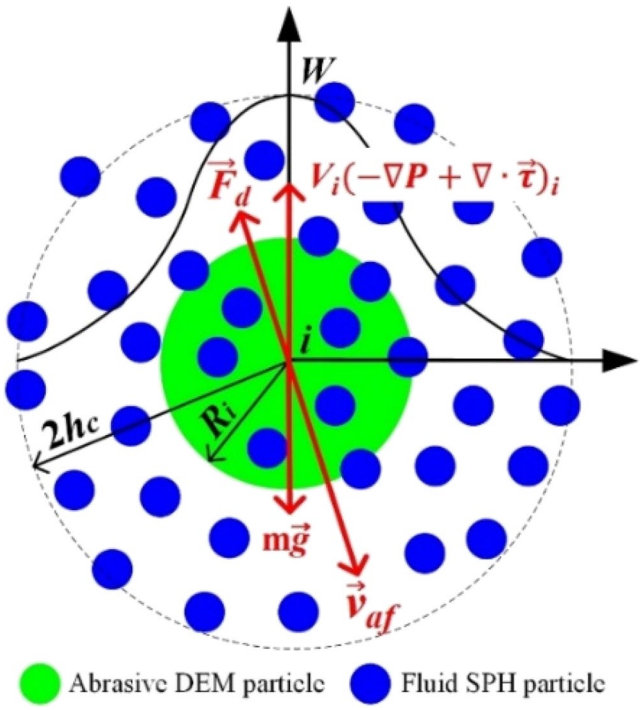


**Figure 7**. SPH-DEM unresolved coupling force for abrasive-fluid interaction.

$$\begin{cases} \epsilon\ominus_i = \frac{\sum_a \epsilon_a V_a W_{ia}(h_c)}{\sum_a V_a W_{ia}(h_c)} \\ \vec{v}_{af} = \bar{v}_f - \vec{v}_i \end{cases}, \tag{45}$$

where $\vec{v}_i$ is the center velocity of DEM particle *i*. The average fluid velocity $\bar{v}_f$ at point *i* can be approximated by the Shepard correction method expressed as:

$$\bar{v}_f = \frac{\sum_a \vec{v}_a V_a W_{ia}(h_c)}{\sum_a V_a W_{ia}(h_c)}, \tag{46}$$

In Eq. (44), $\beta$ is the momentum exchange coefficient between two phases, which is determined by the average porosity $\epsilon_i$[55]:

$$\beta = \begin{cases} 150\frac{(1-\epsilon_i)^2}{\epsilon_i}\frac{\mu_f}{d_i^2} + 1.75(1-\epsilon_i)\frac{\rho_f}{d_i}\left|\vec{v}_{af}\right|\epsilon_i 0.8 \\ 0.75C_d\frac{\epsilon_i(1-\epsilon_i)}{d_i}\rho_f\left|\vec{v}_{af}\right|\epsilon_i^{-2.65}\epsilon_i 0.8 \end{cases}, \tag{47}$$

where $C_d$ is the drag coefficient given by:

$$C_d = \begin{cases} *20l\frac{24}{Re_i}(1+0.15Re_i^{0.687}), Re_i 1000 \\ 0.44, Re_i 1000 \end{cases}, \tag{48}$$

where $Re_i$ is the Reynolds number around DEM particle *i* expressed as:

$$Re_i = \frac{\left|\vec{v}_{af}\right|\epsilon_i\rho_f d_i}{\mu_f}. \tag{49}$$

In order to satisfy Newton's third law, the coupling force $\vec{F}_{f\text{-}a}$ of SPH particle *a* subjected to DEM particles in Eq. (23) is the weighted average of $\vec{F}_{a\text{-}f}$ acting on DEM particles nearby, which can be given by:

$$\begin{cases} \vec{F}_{f-a} = -\frac{m_a}{\bar{\rho}_a}\sum_i \frac{1}{S_i}\vec{F}_{a-f}W_{ai}(h_c) \\ S_i = \sum_b \frac{m_b}{\bar{\rho}_b}W_{bi}(h_c) \end{cases}, \tag{50}$$

where the subscript *b* represents the SPH particle within the coupling radius $R_c$ of DEM particle *i*.

## Time integration scheme

The time step length $\Delta t$ is crucial for the explicit dynamic simulation. If $\Delta t$ is too large, it will result in too few time steps for SPH&DEM particles to come into contact, which affects the numerical stability, and even causes the calculation to abort. If $\Delta t$ is too small, it needs more time steps to simulate the same physical time period, which increases time cost and reduces computational efficiency. For SPH particles, the Courant-Friedrichs-Levy (CFL) condition is adopted, which requires $\Delta t$ to be proportional to the smallest spatial resolution. For DEM particles, $\Delta t$ is related to the normal stiffness coefficient $k_n$ and can be expressed as[56]:

$$\begin{cases} \Delta t = \min\left(\Delta t_{sph}, \Delta t_{dem}\right) \\ \Delta t_{sph} = \min_{\text{ath-particle}}\left(\frac{C_F h_a}{c_a + |\vec{v}_a|}\right) \\ \Delta t_{dem} = \frac{2\pi}{\alpha_{tn}}\sqrt{\frac{m_i}{k_n}} \end{cases}, \tag{51}$$

where $C_F = 0.2$ is the CFL coefficient, $h_a$, $c_a$, and $|\vec{v}_a|$ are the smoothing length, sound velocity, and maximum velocity of the SPH particle, respectively. $\alpha_{tn} = 300$ is the model coefficient, and $m_i$ is the mass of the DEM particle. If the difference between $\Delta t_{sph}$ and $\Delta t_{dem}$ is less than one order of magnitude, the smaller one will be selected as the time step of SPH-DEM coupled model to ensure the numerical stability.

As shown in Eq. (51), the time step $\Delta t_{sph}$ for SPH particles is determined by the sound velocity $c_a$ and the maximum velocity $|\vec{v}_a|$. In this paper, $C_F = 0.2$, $h_a = 1.25d_{ini} = 6.25\times10^{-5}$m, $c_a = 3940$ m/s (sound velocity of OFHC copper), $|\vec{v}_a| = 600$ m/s, and $\Delta t_{sph}$ is calculated as $2.75\times10^{-9}$s. For DEM particles, $\Delta t_{dem}$ is a constant value, which is related to the diameter and material properties. In this paper, $d_{dem} = 0.2$ mm, $\rho_{dem} = 4120$ kg/m$^3$, $E = 248$GPa, $v = 0.3$, and $\Delta t_{dem}$ is calculated as $6.34\times10^{-9}$s. Therefore, considering computational efficiency and numerical stability, the time step is set to $\Delta t = 2.0\times10^{-9}$s.

The flow chat of unresolved SPH-DEM coupled model is shown in Fig. 8, which is implemented by a Fortran code. The leap-frog method is applied for the time integration scheme, and the link-list method is used for neighboring particle-pair searching (NPPS). The internal forces of SPH particles include pressure term $P_a$, viscosity term $\Pi_{ab}^{visc}$& $\pi_{ab}^{art}$, and deviator stress term $\vec{\tau}_a$, which have been shown in Eqs. (23) and (29).

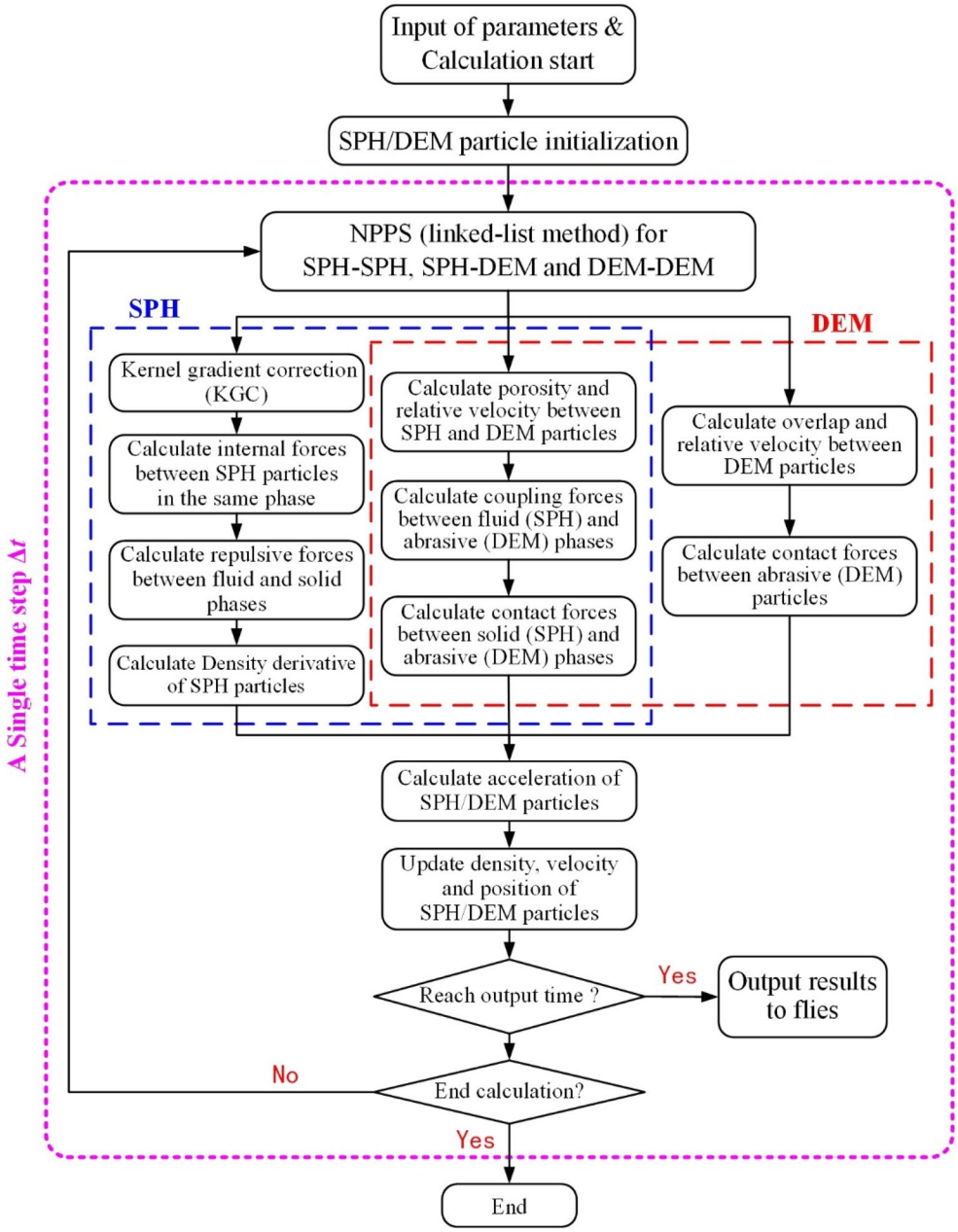


**Figure 8**. Flowchart of unresolved SPH-DEM coupled model for AWJ impact.

## Results and discussion

In this section, several simulation cases of AWJ impact are conducted based on the unresolved SPH-DEM model above, including the single AWJ impact on rigid wall (Sect. 4.1), continuous AWJ impact on ductile materials (Sect. 4.2) and brittle materials (Sect. 4.3).

The 2D AWJ model is shown in Fig. 9, including geometrical parameters (model thickness & width) and AWJ incident parameters (incident angle $\alpha$, incident velocity $v_{jet}$, AWJ diameter $d_{jet}$ and distance between adjacent abrasives in Y direction $y_{dis}$). The geometrical parameters depend on AWJ incident parameters. Fluid SPH particles and abrasive DEM particles are continuously generated at the inlet and exit the computation domain through outlets on both sides to simulate the continuous impact process over a long time scale. In the actual AWJ cutting process, the solid specimen is fixed by surrounding fixtures. Therefore, the left and right sides of the solid model are set as fixed constraints during the simulation process, while the upper and lower boundaries are not constrained.

### Single abrasive water-jet impact on rigid wall

For the unresolved SPH-DEM model, the most critical numerical parameter is the coupling radius $R_c$ between SPH and DEM particles. Two type of particles within $R_c$ interact through the local porosity. If $R_c$ is too small,

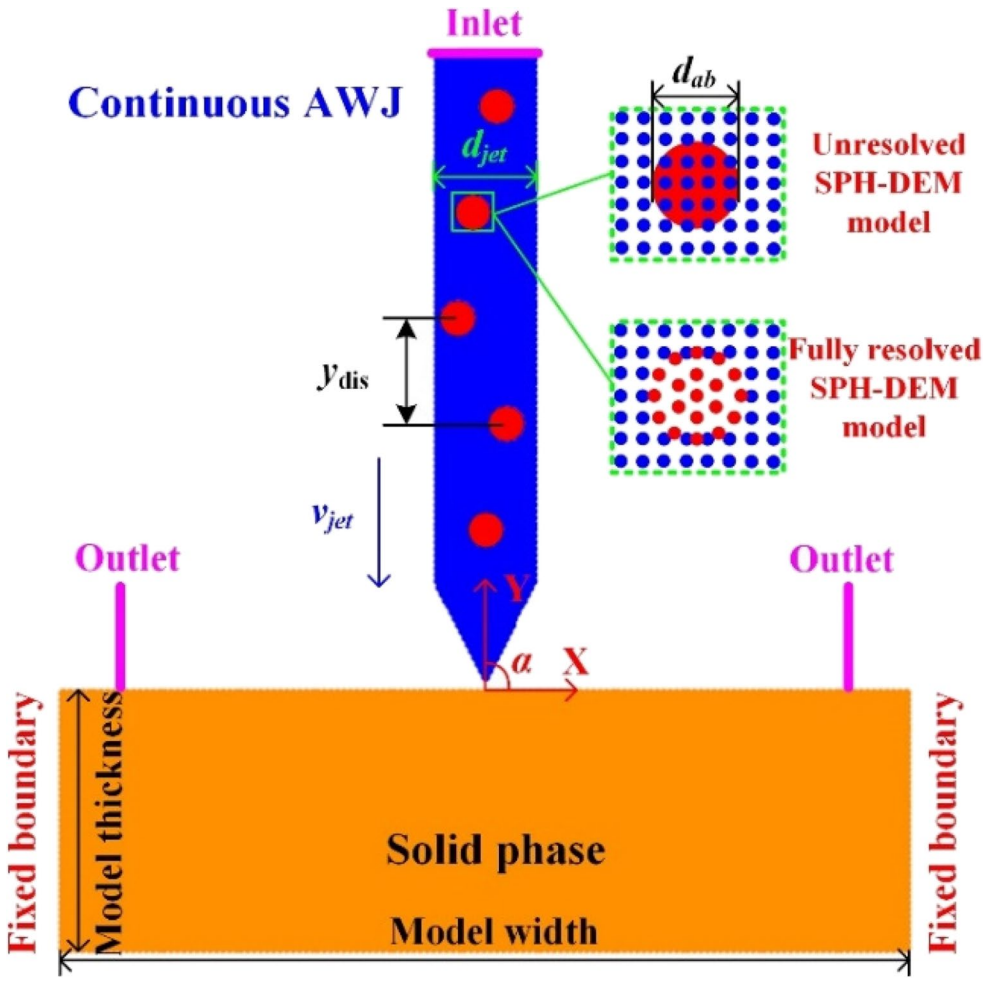


**Figure 9**. Illustration of unresolved SPH-DEM model for continuous AWJ impact.

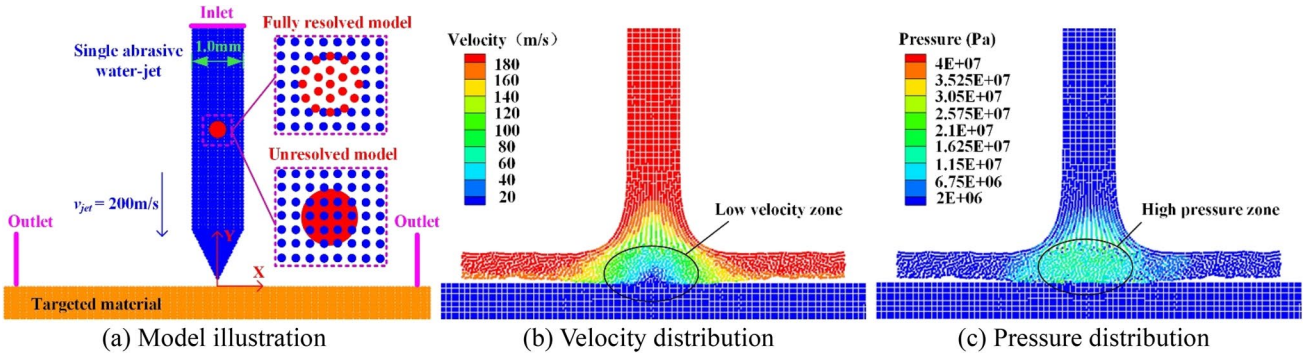


**Figure 10**. Single abrasive water-jet numerical simulation.

the coupling force between abrasive and fluid phases is not enough to reflect the abrasive-fluid interaction. If $R_c$ is too large, the local characteristics of the flow field and the abrasives cannot be captured, and a large amount of calculation is required. In general, $R_c$ should be larger than the diameter of the DEM particle at least, but also small enough to capture the local characteristics of the flow field.

In order to determine the optimal value of $R_c$, a model of single abrasive water-jet impact is established, as shown in Fig. 10(a). The water-jet contains only one abrasive particle to study the motion under the action of fluid SPH particles around. The circular abrasive particle has a diameter of $d_{ab}$ = 0.20 mm, and consists of a group of DEM particles (Fully resolved) or a single DEM particle (Unresolved). The fully resolved SPH-DEM

| Parameter properties and labels | Value |
|---|---|
| Fluid SPH particle parameters | |
| Initial spacing, $d_{ini}$ (mm) | 0.05 |
| Smoothing length, $h$ (mm) | $1.25d_{ini}$ |
| Initial density, $\rho_0$ (kg/m$^3$) | $1.0\times10^3$ |
| Dynamic viscosity, $\mu_f$ (Pa·s) | $1.0\times10^{-3}$ |
| Time step, $\Delta t$ (s) | $2.0\times10^{-9}$ |
| Rigid abrasive DEM particle parameters | |
| Density, $\rho_{dem}$ (kg/m$^3$) | $4.12\times10^3$ |
| Diameter, $d_{dem}$ (mm) | 0.20 |
| Young's modulus, $E$ (GPa) | 248 |
| Poisson ratio, $\upsilon$ | 0.3 |
| Friction coefficient, $\mu$ | 0.3 |
| Restitution coefficient, $e$ | 0.6 |
| AWJ incident parameters | |
| Distance between adjacent abrasives in Y direction, $y_{dis}$ (mm) | 1.0 |
| Jet diameter, $d_{jet}$ (mm) | 1.0 |
| Incident velocity, $v_{jet}$ (m/s) | 200 |
| Incident angle, $\alpha$ (°) | 90 |
| Nozzle traverse speed, $v_{tran}$ | 0 |

**Table 4**. Numerical parameters for continuous AWJ impact simulation.

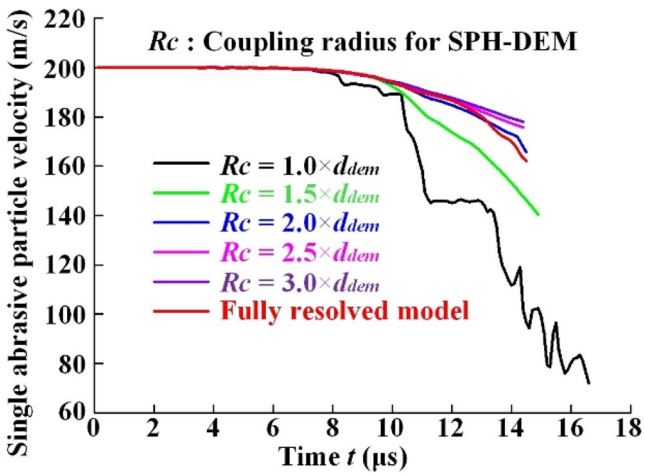


**Figure 11**. Time history of single abrasive's velocity (Before colliding with rigid solid wall).

model for AWJ impact has been discussed in our previous research[57]. The solid phase is set as the rigid body, ignoring the deformation during the impact process. Other numerical parameters are listed in Table 4.

When the water-jet impacts the solid surface, the shape of water-jet undergoes a drastic change and ultimately leaves from the outlets on both sides. The velocity and pressure distribution of fluid phase, once the water-jet shape has stabilized, is shown in Fig. 10(b) and 10(c). At the center of the water-jet flow, the fluid SPH particles have the highest pressure and the lowest velocity. It indicates that as the abrasive particles gradually approach the solid surface from inlet, the pressure and drag effects from the fluid phase located at the center are greatly enhanced, causing the abrasive particles to decelerate before they contact with the solid phase.

Time history of the single abrasive particle's velocity is shown in Fig. 11, for the time period from $t=0$ to contact with the rigid solid wall. In the fully resolved model, the velocity of abrasive particle in contact with the solid is about 162 m/s. For the unsolved model, the abrasive contact velocity is affected by the coupling radius $R_c$. When $R_c = 1.0d_{dem}$, the abrasive velocity fluctuates in a stepwise manner, with greater amplitude. Due to the small size of $R_c$, the number of fluid SPH particles interacting with the single abrasive DEM particle is insufficient, making it difficult to reflect the actual flow of particles. With the increase of $R_c$, the variation of particle velocity curve tends to be gentle, and the particle contact velocity gradually increases. When $R_c \geq 2.5d_{dem}$, due to the limitation of jet diameter $d_{jet} = 1.0$ mm, increasing $R_c$ has little effect on the simulation results, so the coincidence degree of the curves is relatively high. The particle contact velocity is about 166 m/s at $R_c = 2.0d_{dem}$, which is the

closest to the fully resolved model, and the curve is basically consistent. Therefore, the coupling radius $R_c$ of the unresolved SPH-DEM model for AWJ simulation is selected as $R_c = 2.0d_{dem}$.

## Continuous AWJ impact on ductile materials

*Effect of impact time T*

In this section, the OFHC copper is selected as the ductile material, and the material parameters are listed in Table 2. The simulation result of ductile surface evolution process by continuous AWJ impact is shown in Fig. 12. The incident velocity $v_{jet}$ is 500 m/s, and other numerical parameters are listed in Table 4.

When impact time $T = 2.5$ms, a series of discontinuous pits appear on the ductile surface, as show in Fig. 12(a). With the increase of $T$, these smaller pits gradually merge into a bigger crater, and the initial cross-section profile of the crater is V-shaped, as show in Fig. 12(b). When $T = 10.0$ms, the crater develops to the material interior, and the cross-section profile changes constantly, eventually transforming into U-shape at $T = 30.0$ms, as show in Fig. 12(c ~ e). Subsequently, the crater width is basically unchanged, while the crater depth continues to increase, as show in Fig. 12(f ~ h). Figure 13 shows the time history of ductile surface erosion process, which can be divided into three stages. In Fig. 13(a), Stage One ($0 \le T < 3.2$ms) is the equivalent plastic strain accumulation stage. When AWJ contacts the ductile surface at $T = 0$, the plastic deformation occurs, and the equivalent plastic strain begins to accumulate. Stage Two ($3.2 \le T < 12.5$ms) is the erosion crater formation stage. The cross-section profile of the crater is constantly changing, forming the V-shaped first, and then transitioning to the U-shaped. The erosion mass rate of the ductile material is unstable. Stage Three ($T \ge 12.5$ms) is the stable erosion stage. The erosion mass rate is constant, and the crater begins to develop inside the material. The cross-section shape of the crater is no longer changed (U-shaped), but the size gradually increases. The erosion mechanism of AWJ on ductile materials is the material failure caused by plastic strain accumulation.

Figure 13(b) shows the relationship between the crater size and the impact time. When $T < 10.0$ms, the crater width $C_w$ increases sharply, while the crater depth $C_d$ increases slightly. During this period (in Stage One and

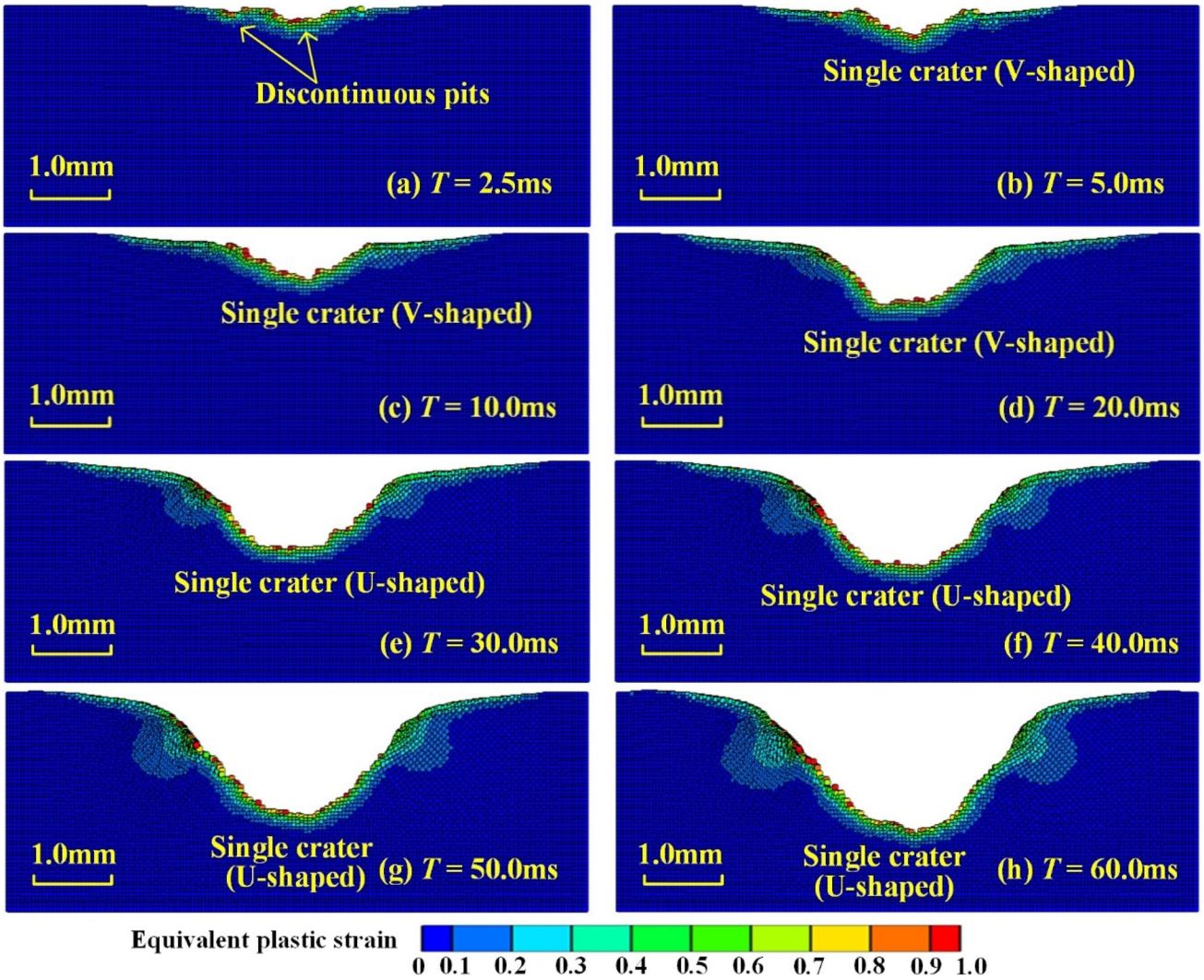


**Figure 12**. Evolution of ductile surface evolution by continuous AWJ impact.

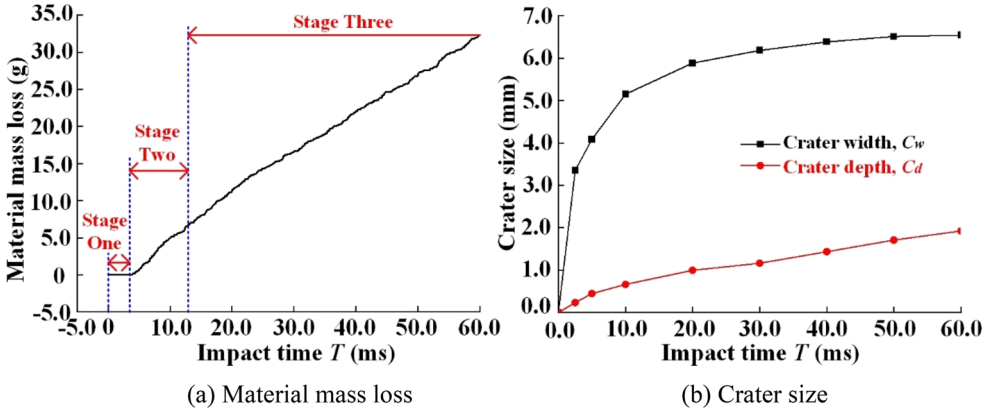


**Figure 13**. Time history of ductile surface erosion by continuous AWJ impact.

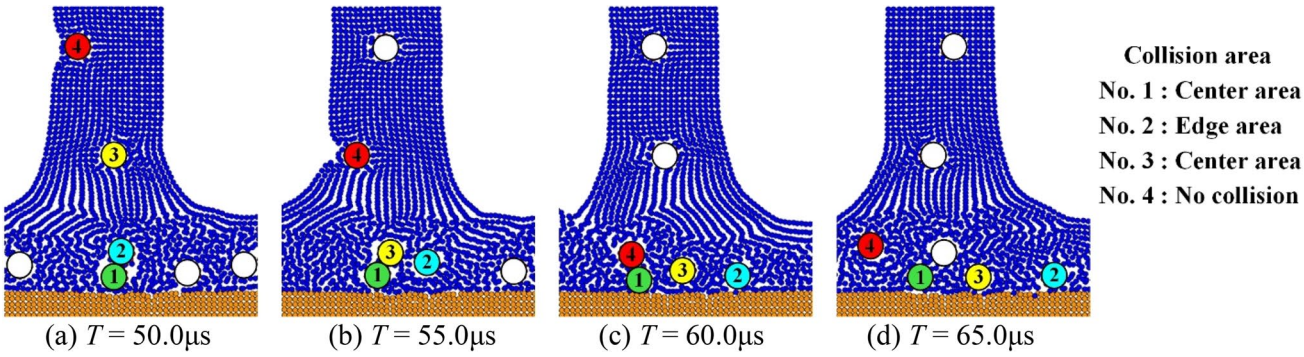


**Figure 14**. Motion trajectory of abrasives at center area.

Two), the ductile surface is basically intact and no significant material removal occurs. When $20.0 \le T < 50.0$ms, $C_w$ increases less rapidly, which is in the stable erosion stage (Stage Three). When $T \ge 50.0$ms, $C_w$ is basically unchanged, while $C_d$ increases linearly during the whole erosion process. It can be seen that as the impact time increases, the erosion area no longer extends to both sides, but develops deeper inside the material.

The abrasive moves by the contact of fluid phase, targeted material, and other abrasives, as shown in Fig. 14. Abrasive No.1 located at the center area is embedded into the ductile surface under the squeezing effect of water-jet, and collides with the subsequent abrasives No.2 ~ 4. The initial position of abrasive No.2 is near the center area. After colliding with abrasive No.1, abrasive No.2 deviates and finally contacts with the ductile surface far from the center area, which expands the erosion region. Abrasive No.4 does not touch the ductile surface, but flows to the outlet under the action of fluid phase and other abrasives. It can be seen from Fig. 10(a) that the AWJ has the lowest velocity in the center area, causing the abrasives to gather and collide. This is the main reason for the sharp increase in the crater width during Stage One and Two in Fig. 13(b).

In the same incident condition ($v_{jet} = 500$ m/s and $T = 30.0$ms), the simulation results of OFHC copper surface erosion by pure water-jet and abrasive water-jet impact are shown in Fig. 15. Under the continuous impact of pure water-jet, local plastic deformation and a small amount of material removal occur on the ductile surface, resulting in a wide and shallow crater with 6.89 mm in width and 0.54 mm in depth. Under the continuous impact of AWJ, a large amount of material removal occurs, and the crater is narrow and deep with a U-shaped of 6.18 mm in width and 1.16 mm in depth. Therefore, the erosion ability of AWJ to the targeted material is much greater than that of pure water-jet. As can be seen from Fig. 15(b), the water-jet not only accelerates the abrasives, but also cleans the material surface. The abrasives and the material debris located at the crater bottom flow to outlet on both sides by the continuous water-jet, which reduces the obstruction of the accumulation of abrasives and materials on impact, and provides space for subsequent abrasives.

*Effect of incident velocity $v_{jet}$*

The incident velocity $v_{jet}$ is defined as the flow velocity of AWJ at the inlet, which is one of the key factors affecting jet erosion ability. In the actual AWJ cutting process, the $v_{jet}$ value cannot be directly set, and it is determined by adjusting the working pressure $P$ of the booster cylinder. The relationship between $P$ and $v_{jet}$ can be solved by Bernoullis's equation, expressed as[58]:

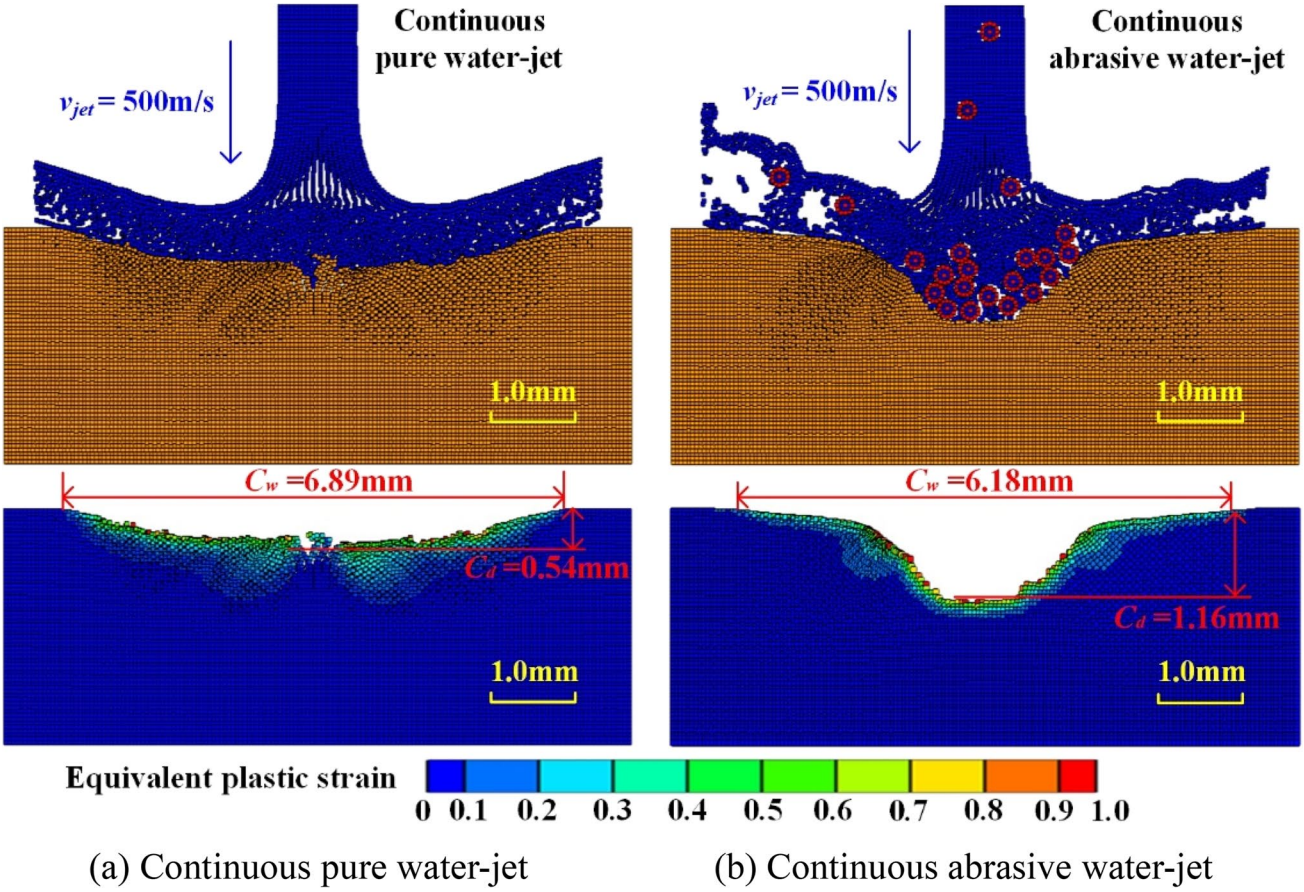


**Figure 15**. Simulation results of OFHC copper surface erosion by water-jet impact in two types.

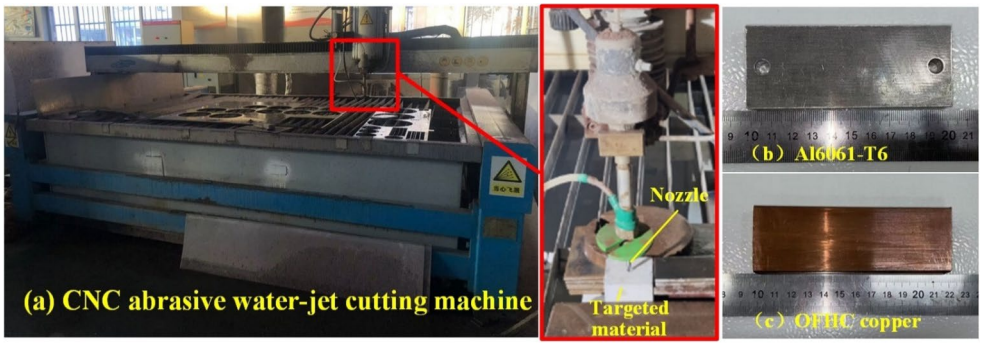


**Figure 16**. AWJ erosion experimental system and ductile specimens.

$$v_{jet} = \kappa\sqrt{\frac{2P}{\rho}}, \tag{52}$$

where $\rho = 1000$ kg/m$^3$ is the density of liquid medium. $\kappa$ is the volume efficiency ranging from 0.7 to 0.85[58]. In this study, $\kappa = 0.7$, and Eq. (52) can be rewritten as:

$$v_{jet} = 31.3\sqrt{P}. \tag{53}$$

The SPH-DEM model proposed in this study is verified by AWJ impact experiment, which is carried out by a gantry CNC abrasive water-jet cutting machine, as shown in Fig. 16(a). The OFHC Copper and Al6061-T6 specimens are selected as the targeted ductile materials with a dimension of 120*40*8 mm and 100*40*8 mm,

as shown in Fig. 16(b) and 16(c). Several cases are conducted through the impact experiment and the numerical model, and the specific experimental parameters are shown in Table 5.

The crater profiles obtained from impact experiment and simulation results under different incident velocities are shown in Fig. 17. Among them, the targeted material of Cases 1 ~ 3 (Fig. 17(a ~ c)) are OFHC copper, and Cases 4 ~ 6 (Fig. 17(d ~ f)) are Al6061-T6. The crater profile images are taken with a microscope (maximum magnification is 1500X). Under the continuous AWJ impact, craters with different sizes are produced on the surface of two ductile materials. Due to the lower hardness of OFHC copper (35 ~ 45HB) compared to the material (90 ~ 95HB), material accumulation occurs on both sides of the crater for copper, while there is no obvious material accumulation for Al6061-T6. These phenomena are also reflected in the simulation process. Besides, the experiment and simulation results are basically the same, indicating that the unresolved SPH-DEM coupled model proposed in this study can accurately simulate the plastic deformation and material removal phenomena of the ductile materials, which can be used for AWJ study.

The crater profiles obtained from simulation results for copper and Al under different incident velocities are shown in Fig. 18. In these cases, the nozzle transverse velocity $v_{tran} = 0$, the incidence angle $\alpha = 90°$, and the impact time $T = 30.0$ms. With the increase of $v_{jet}$, the crater depth $C_d$ and crater width $C_w$ increase obviously. The relationship between $C_d$ and $v_{jet}$ is basically linear, which is similar to the result of Ti6Al4V material erosion process by AWJ impact in Ref[58]. , as shown in Fig. 18(c). While the grow of $C_w$ gradually slows down and tends to a stable value, the crater length-diameter ratio $C_d$ / $C_w$ increases. In Fig. 18(a) and (b), the erosion effect of AWJ is concentrated at the crater bottom, and the crater profile gradually develops from a V-shaped to a U-shaped with the increase of $v_{jet}$. Due to the lower density of Al6061-T6 material, although it has higher hardness, the erosion resistance is still weaker than OFHC copper, so the crater size of Al6061-T6 is significantly larger with the same incident velocity.

*Effect of abrasive mass flow rate M*

Abrasive mass flow rate $M$ is also one of the key factors affecting material removal and crater size. Under a certain working pressure, $M$ is indirectly controlled by the opening of the sand tank outlet, so the abrasive mass flow rate cannot be set precisely during AWJ impact experiment. In the SPH-DEM model proposed in this study, a liquid column with length $y_{dis}$ and width $d_{jet}$ is generated at the inlet every $y_{dis}/v_{jet}$ seconds, which is composed of SPH particles. Each liquid column contains a randomly distributed abrasive (DEM particle), as shown in Fig. 9. The relationship between abrasive volume fraction $\zeta$ and liquid column length $y_{dis}$ can be obtained as follows:

$$\zeta = \frac{V_a}{y_{dis} \cdot d_{jet}} \times 100\%, \tag{54}$$

where $V_a$ is the volume occupied by a single abrasive particle. The expression of abrasive mass flow rate $M$ is given by:

$$M = \rho_{dem} v_{jet} d_{jet} \zeta = \rho_{dem} v_{jet} \cdot \frac{V_a}{y_{dis}}, \tag{55}$$

The relationship between $M$ and $y_{dis}$ is shown in Fig. 19. Therefore, $M$ can be accurately determined from the value of $y_{dis}$ in the simulation process.

The simulation results of the profiles and sizes of the crater on OFHC copper surface with different abrasive mass flow rates are shown in Fig. 20. In these cases, $v_{tran} = 0$, $\alpha = 90°$, $v_{jet} = 350$ m/s, and $T = 60.0$ms, the crater size increases with the increase of $M$. Among them, $C_w$ is more affected, while $C_d$ is less affected. When $M \geq 0.07$ kg/s, $C_d$ is basically a constant value, resulting in a decrease in $C_d$ / $C_w$, as shown in Fig. 20(b). The crater profile gradually develops from a U-shaped to a V-shaped with the increase of $M$. The collision of abrasive particles may be the main reason, as shown in Fig. 21. When $M \geq 0.07$ kg/s, the abrasives accumulate at the crater bottom and collide each other, making the subsequent abrasives contact the ductile surface far from the center area, or unable to make contact. It indicates that in the practical application of AWJ cutting ductile materials, it is not possible to infinitely increase the material erosion rate and crater size by increasing the abrasive mass flow rate. Excessive abrasive mass flow rate will greatly increase the crater width, affect the kerf surface quality, and cause blockage of the abrasive pipe, which will reduce the service life of the equipment.

| Case | Ductile material | Working pressure $P$ (MPa) | Incident velocity $v_{jet}$ (m/s) | Sand ratio $\zeta$ (%) | Traverse speed $v_{tran}$ (mm/min) | Stand-off distance H (mm) |
|---|---|---|---|---|---|---|
| 1 | OFHC copper | 150 | 383 | 30 | 2000 | 2 |
| 2 | OFHC copper | 200 | 443 | 30 | 2000 | 2 |
| 3 | OFHC copper | 250 | 495 | 30 | 2000 | 2 |
| 4 | Al6061-T6 | 150 | 383 | 30 | 2000 | 2 |
| 5 | Al6061-T6 | 200 | 443 | 30 | 2000 | 2 |
| 6 | Al6061-T6 | 250 | 495 | 30 | 2000 | 2 |

**Table 5**. Experimental parameters with different impact velocities on ductile surface.

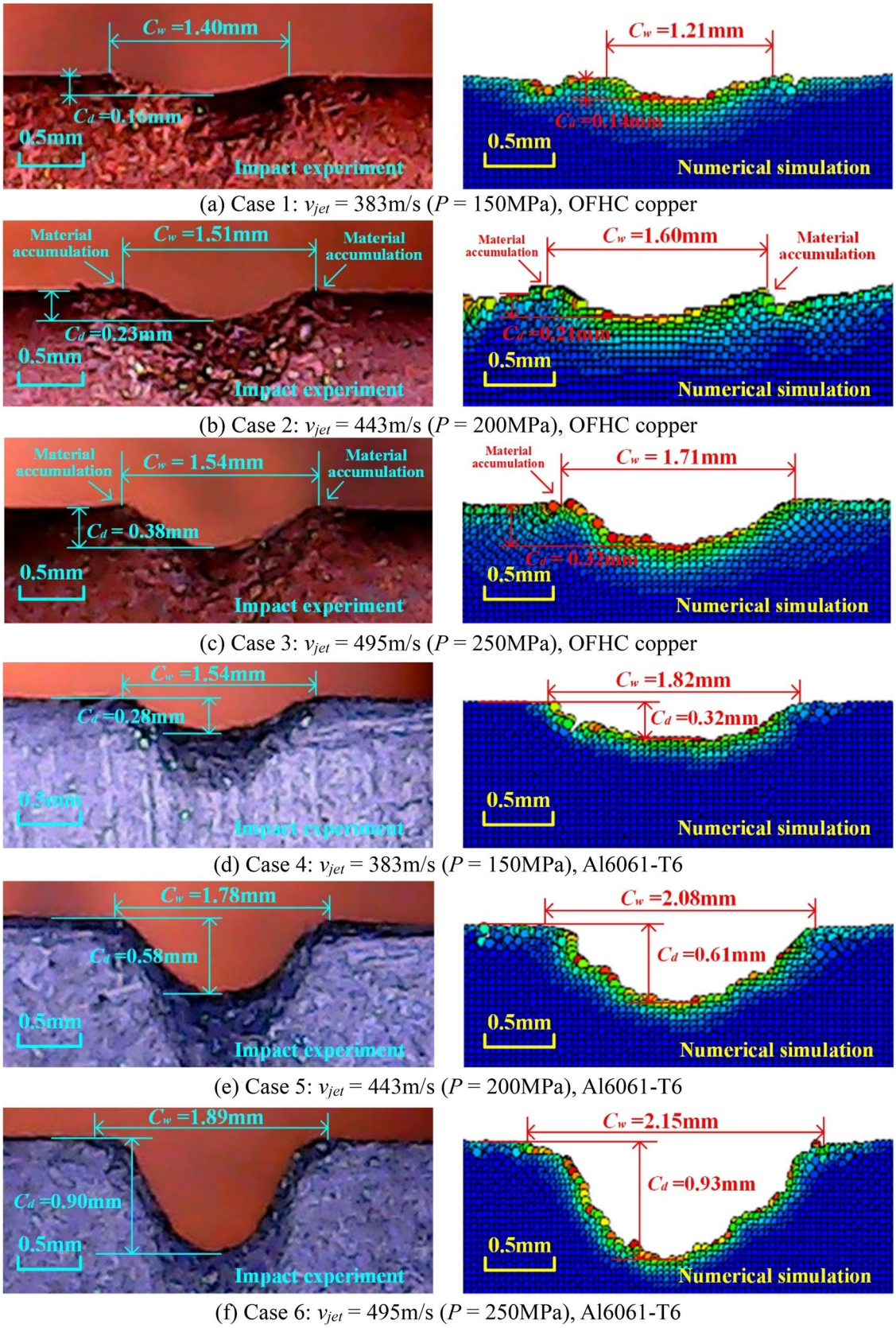


**Figure 17**. Experiment and simulation results of crater profile on ductile surface with different incident velocities.

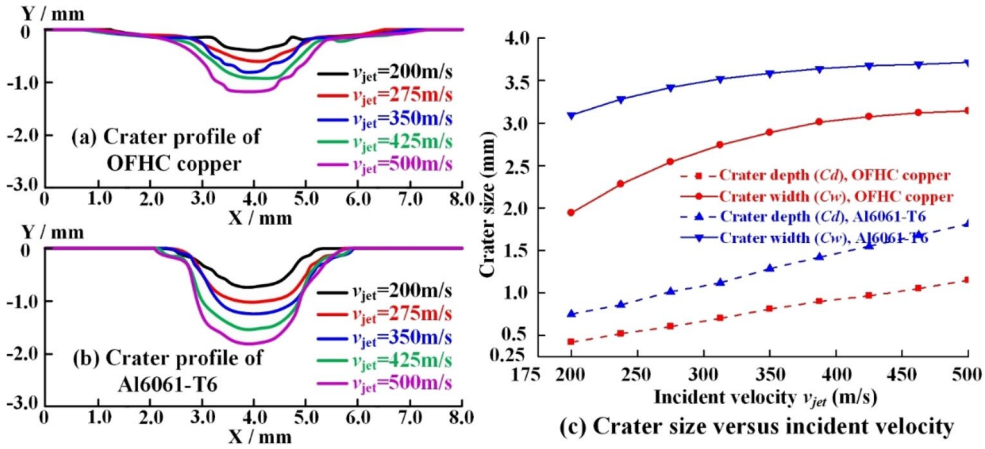


**Figure 18**. Simulation results of crater on ductile surface with different incident velocities.

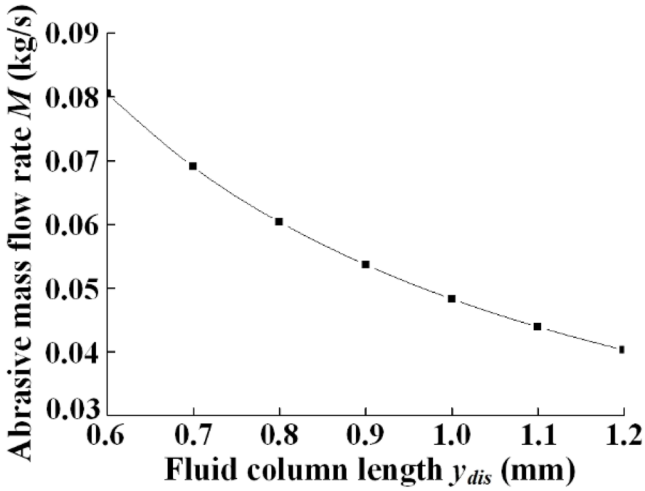


**Figure 19**. Relationship between abrasive mass flow rate and fluid column length.

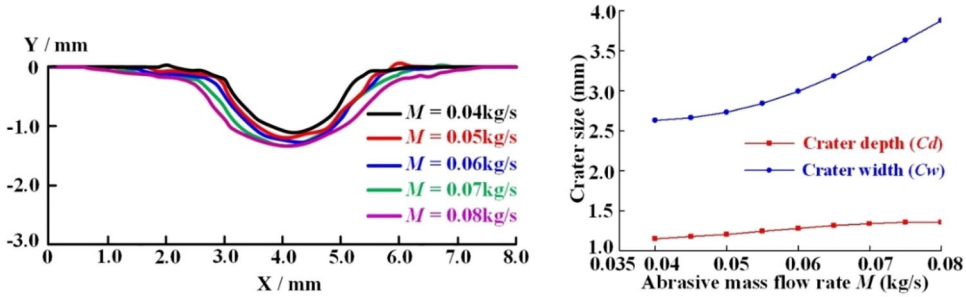


(a) Crater profile (b) Crater size versus abrasive mass flow rate

**Figure 20**. Simulation results of crater on OFHC copper surface with different abrasive mass flow rates.

## Continuous AWJ impact on brittle materials

*Effect of impact time T*

In this section, the red sandstone is selected as the brittle material, and the material parameters are listed in Table 3. The simulation result of brittle surface evolution process by continuous AWJ impact is shown in Fig. 22. The incident velocity $v_{jet}$ is 400 m/s, and other numerical parameters are listed in Table 4.

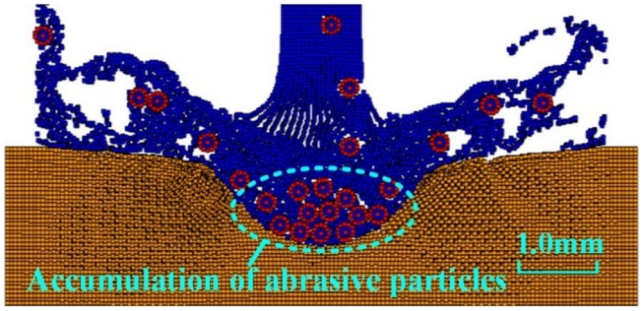


**Figure 21**. Accumulation of abrasive particles at the crater bottom ($M = 0.07$ kg/s).

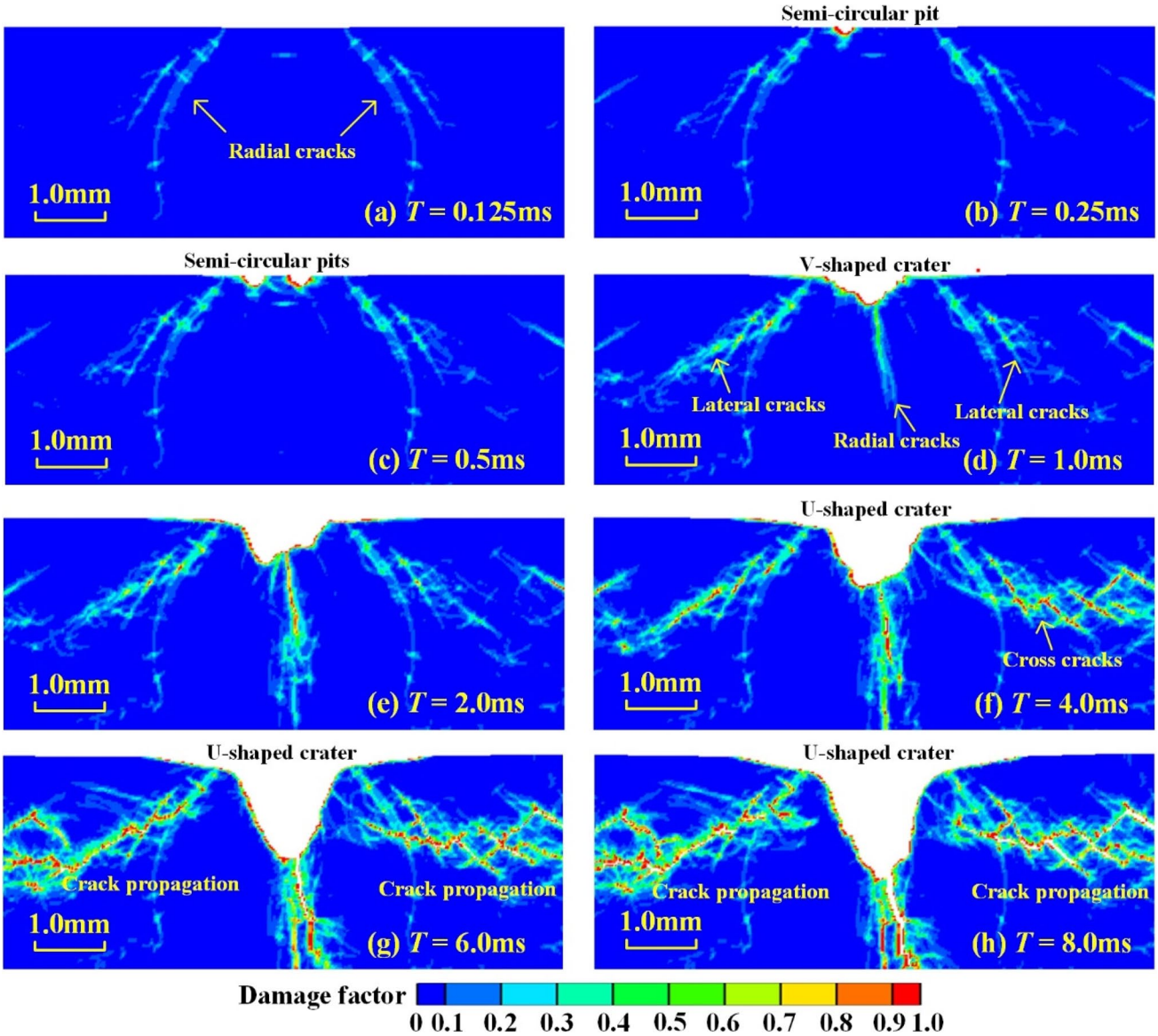


**Figure 22**. Evolution of brittle surface evolution by continuous AWJ impact.

At the instant of contact between water-jet and brittle surface ($T = 0.125$ms), radial cracks appear on both sides of the water-jet edge. These cracks are generated by the action of water hammer pressure before the abrasive particles contact the brittle surface. With the continuous impact of water-jet, the water hammer pressure at the center area rapidly decreases to the stagnation pressure ($P_s = \frac{1}{2}\rho v_{jet}^2$), so the radial crack number no longer

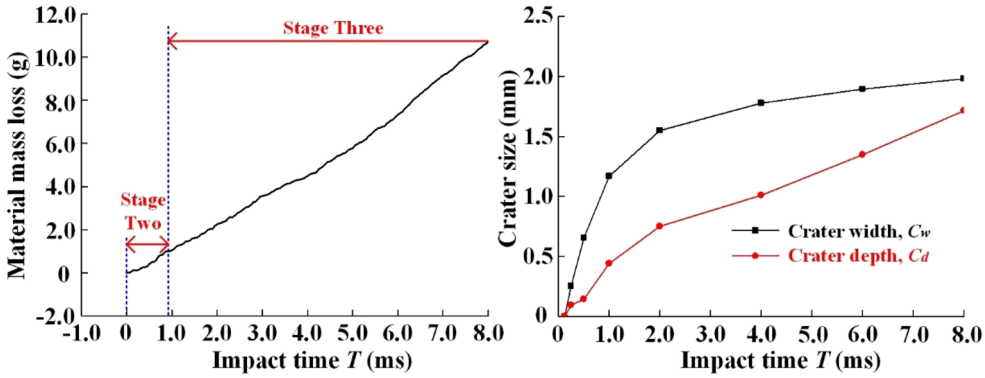


(a) Material mass loss (b) Crater size

**Figure 23**. Time history of brittle surface erosion by continuous AWJ impact.

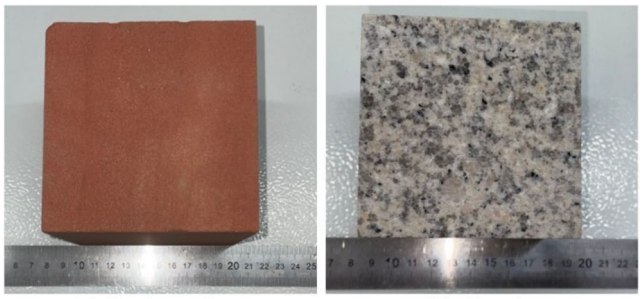

(a) Red sandstone (b) Granite

**Figure 24**. Brittle specimens for AWJ impact experiment.

increases, but gradually spreads inside the brittle material. The abrasive particles contact with the brittle surface at $T = 0.25$ms, resulting in a semi-circular pit, and the radial cracks gradually develop to both sides, forming new lateral cracks. With the continuous impact of abrasive particles, several surface pits gradually merge into a large V-shaped crater at $T = 1.0$ms, and new radial cracks appear at the crater bottom. The V-shaped crater expands rapidly into the targeted material along direction of the bottom radial cracks at $T > 2.0$ms. The crater section profile changed constantly, and the lateral cracks on crater sides continue to increase and cross each other. The crater changes from V-shaped to U-shaped at $T = 4.0$ms. The network cracks are generated at the same time, which greatly increases the damage area. When $T > 4.0$ms, the crater depth continues to expand, while the crater width no longer increases. The lateral cracks on both sides begin to spread towards the brittle surface. When the lateral cracks extend to the surface, the brittle material is fragmented, forming large fragments and material removal.

Figure 23(a) shows the time history of brittle material mass loss during AWJ impact process. Material failure and removal occurs at the moment of AWJ impact, without undergoing the equivalent plastic strain accumulation stage (Stage One). Instead, it directly enters the erosion crater formation stage (Stage Two), which is different from the ductile materials. When $T > 0.9$ms, the erosion process enters the stable erosion stage (Stage Three), and the brittle material mass loss increases linearly with the impact time. Figure 23(b) shows the time history of the crater size. When $T \leq 1.0$ms, the crater profile is a series of discontinuous surface pits. The crater width $C_w$ increases rapidly, while the crater depth $C_d$ increases by steps. When $T > 1.0$ms, the increasing trend of $C_w$ and $C_d$ gradually decreases. When $T > 4.0$ms, $C_w$ is generally unchanged, and $C_d$ increases linearly with the impact time. For brittle materials, it can be concluded that the relationship between the crater width and the impact time is similar to that of the ductile materials. However, the variation of crater depth is mainly reflected in the initial erosion stage (Stage One and Two). The erosion mechanism of AWJ on brittle materials is the propagation and diffusion of cracks inside the material caused by repeated impact of abrasive particles.

*Effect of incident velocity $v_{jet}$*

In this section, the red sandstone and granite specimens are selected as the targeted brittle materials with sizes of 100*100*100 mm and 80*80*80 mm, respectively, as shown in Fig. 24. Several impact experiment cases are conducted to verify the numerical model, and the specific experimental parameters are shown in Table 6.

The impact experiment and numerical simulation results of the crater profiles with different incident velocities are shown in Fig. 25. Among them, the targeted material of Cases 1 ~ 3 (Fig. 25(a ~ c)) are red sandstone, and Cases 4 ~ 6 (Fig. 25(d ~ f)) are granite. U-shaped craters with different depths appear on the sandstone surface,

| Case | Brittle material | Working pressure $P$ (MPa) | Incident velocity $v_{jet}$ (m/s) | Sand ratio ζ (%) | Traverse speed $v_{tran}$ (mm/min) | Stand-off distance H (mm) |
|---|---|---|---|---|---|---|
| 1 | Red sandstone | 100 | 313 | 30 | 1500 | 2 |
| 2 | Red sandstone | 120 | 343 | 30 | 1500 | 2 |
| 3 | Red sandstone | 140 | 370 | 30 | 1500 | 2 |
| 4 | Granite | 100 | 313 | 30 | 1500 | 2 |
| 5 | Granite | 120 | 343 | 30 | 1500 | 2 |
| 6 | Granite | 140 | 370 | 30 | 1500 | 2 |

**Table 6**. Experimental parameters with different impact velocities on brittle surface.

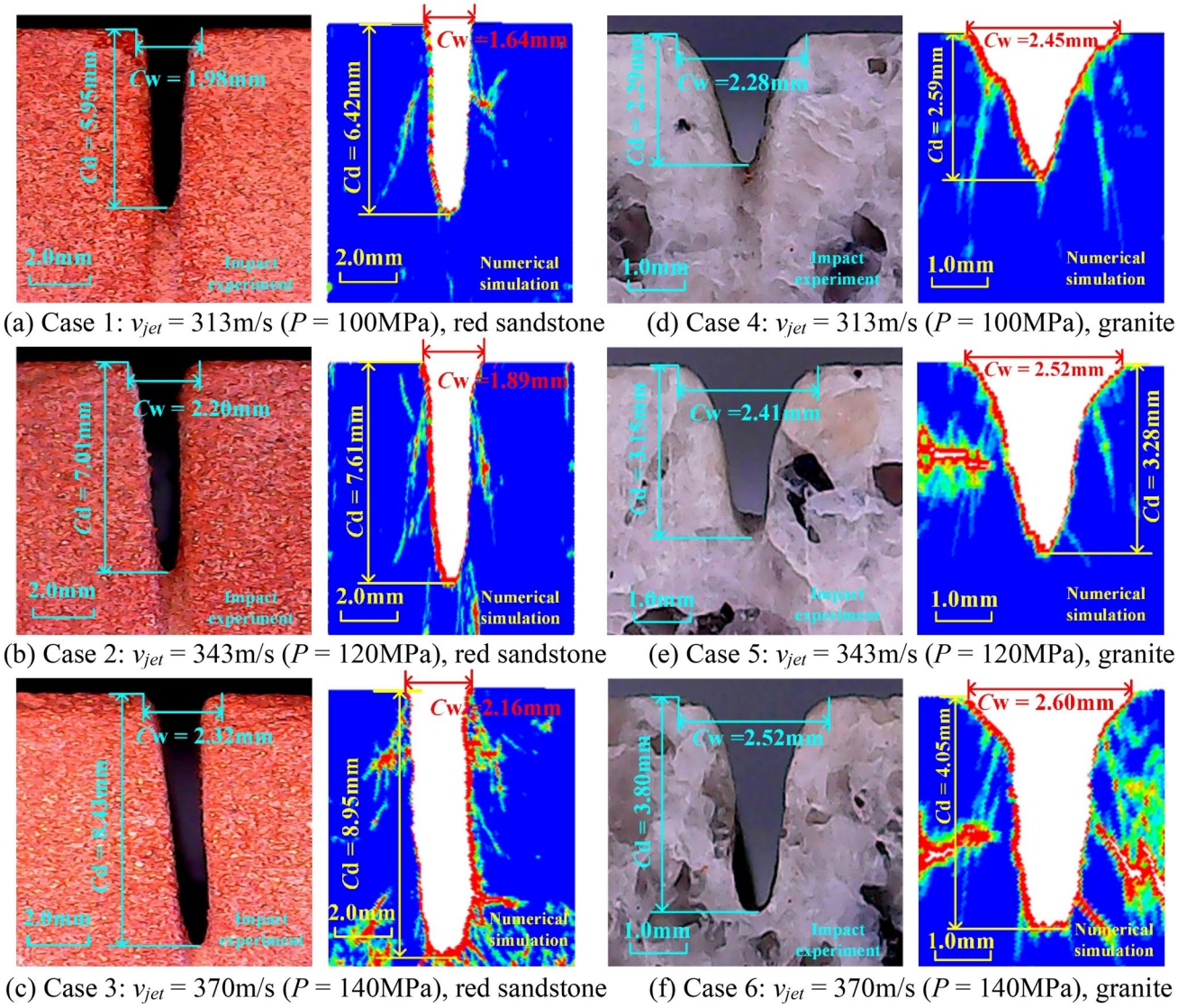


(a) Case 1: $v_{jet}$ = 313m/s ($P$ = 100MPa), red sandstone (d) Case 4: $v_{jet}$ = 313m/s ($P$ = 100MPa), granite

(b) Case 2: $v_{jet}$ = 343m/s ($P$ = 120MPa), red sandstone (e) Case 5: $v_{jet}$ = 343m/s ($P$ = 120MPa), granite

(c) Case 3: $v_{jet}$ = 370m/s ($P$ = 140MPa), red sandstone (f) Case 6: $v_{jet}$ = 370m/s ($P$ = 140MPa), granite

**Figure 25**. Experiment and simulation results of crater profile on brittle surface with different incident velocities.

while the craters on the granite surface gradually transit from the initial V-shaped to U-shaped with the increase of incident velocity $v_{jet}$. When $v_{jet}$.= 313 m/s (Fig. 25(a, d)), the water-jet produces only two radial cracks on both sides, which are generated by the action of water hammer pressure at the contact moment. None of new radial cracks can be observed during the subsequent impact process. When $v_{jet}$.= 343 m/s (Fig. 25(b, e)), more radial and lateral cracks are produced on both sides. When $v_{jet}$.= 370 m/s (Fig. 25(c, f)), new radial and lateral cracks appear at the crater bottom, and these cracks continue to expand to the material interior, greatly increasing the damage area. In these experiment cases, the shapes of the crater profile of two brittle materials are generally

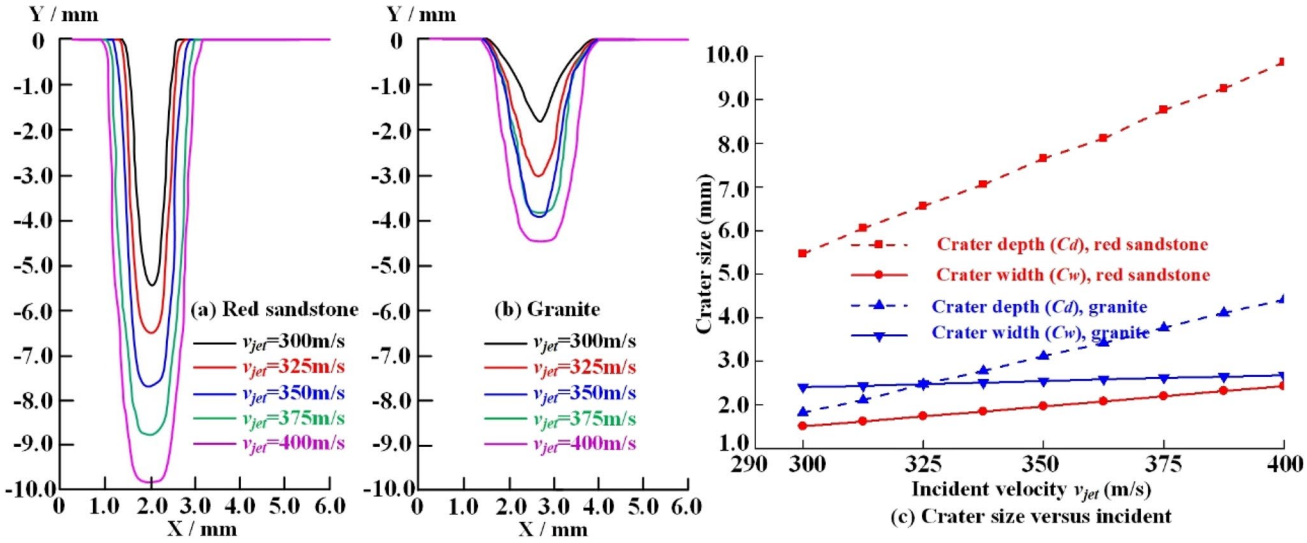


**Figure 26**. Simulation results of crater on brittle surface with different incident velocities.

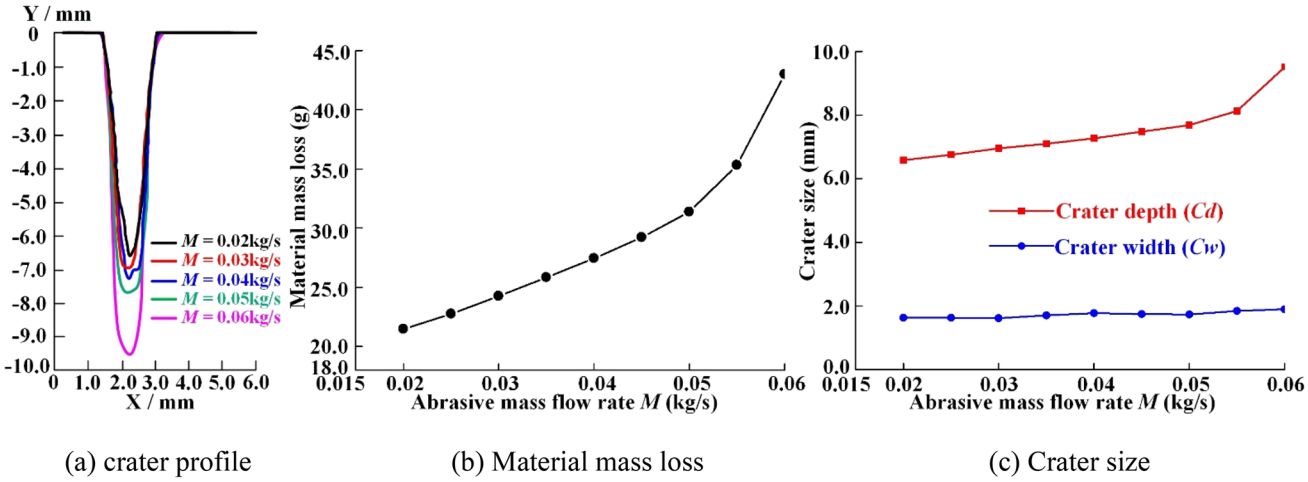


**Figure 27**. Simulation results of crater on red sandstone surface with different abrasive mass flow rater.

consistent with the simulation results, indicating that the numerical model proposed in this study can accurately simulate the crack propagation and surface fragmentation of the brittle materials by AWJ impact.

The simulation results of the profiles and sizes of the crater with different incident velocities are shown in Fig. 26. In these cases, the nozzle transverse velocity $v_{tran} = 0$, the incidence angle $\alpha = 90°$, and the impact time $T = 30.0$ms. When $v_{jet} > 325$ m/s, the profile at the crater bottom gradually expands from a sharp point to a straight line segment, as shown in Fig. 26(a) and (b), indicating that the cross section shape of the crater changes from V-shaped to U-shaped with the increase of $v_{jet}$. The crater depth $C_d$ and crater width $C_w$ increase linearly with $v_{jet}$. Due to the absence of material accumulation on both sides, the growth rate of $C_d$ is significantly greater than that of $C_w$, which is different from the ductile materials. Although the density of red sandstone and granite is similar, the compressive strength of red sandstone is obviously smaller than that of granite, so the erosion resistance of red sandstone is weaker. Besides, $v_{jet}$ as well as crater size of sandstone is obviously larger with the same incident velocity, as shown in Fig. 26(c).

*Effect of abrasive mass flow rate M*

The simulation results of the crater profiles on red sandstone surface with different abrasive mass flow rates are shown in Fig. 27(a). In these cases, $v_{tran} = 0$, $\alpha = 90°$, $v_{jet} = 350$ m/s, and $T = 30.0$ms. When the abrasive mass flow rate $M$ increases from 0.02 kg/s to 0.06 kg/s, the crater depth $C_d$ increases from 6.58 mm to 9.51 mm. By comparison, the crater width $C_w$ fluctuates around 1.73 mm with no significant change. Compared with $C_w$, $C_d$ is more affected by $M$, leading to an increase in $C_d$ / $C_w$. The crater profile gradually develops from V-shaped to U-shaped with the increase of $M$, which is different from the erosion process of ductile materials. Figure 27(b) and (c) show the relationship between the brittle material mass loss, the crater size and the abrasive mass flow

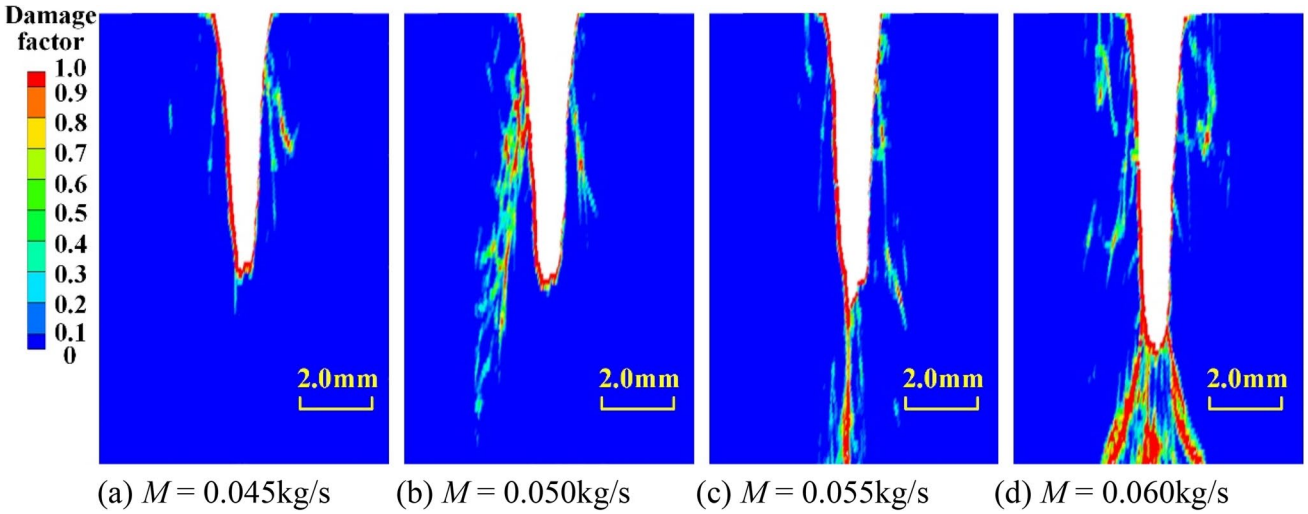


**Figure 28**. Damage distribution inside red sandstone with different abrasive mass flow rates.

rate. With the increase of $M$, the variation law of the mass loss depends on the crater depth $C_d$. When $M \leq 0.055$ kg/s, the brittle material mass loss and $C_d$ increase linearly with the increase of $M$. However, there is a significant increase in above two parameters when $M > 0.055$ kg/s, which can be analyzed through the damage distribution inside the brittle material, as shown in Fig. 28.

It can be seen from Fig. 28(a, b) that with the increase of $M$, the length of radial cracks on both sides of the crater increases significantly. When $M = 0.055$ kg/s, a radial crack appears at the crater bottom, which spreads to the interior along the incident direction of AWJ, as shown in Fig. 28(c). When $M$ increases to 0.060 kg/s, both the crack number and the crater depth at the bottom increase significantly, resulting in a substantial increase in the damage area, as shown in Fig. 28(d). The above phenomenon indicates that there is a threshold of abrasive mass flow rate $M_{cri}$ during the AWJ impact process on brittle materials. If $M \leq M_{cri}$, no radial cracks are generated at the crater bottom, and the crater depth shows a linear increasing relationship with $M$. If $M > M_{cri}$, radial cracks appear at the crater bottom, the material mass loss and crater depth increase greatly, even causing the brittle material to fracture. Therefore, in the process of AWJ cutting, the abrasive mass flow rate should be controlled below $M_{cri}$. While for the process of rock breaking, increasing the abrasive mass flow rate above $M_{cri}$ can significantly increase the drilling speed. In the simulation cases involved in this section, the $M_{cri}$ value is 0.055 kg/s.

## Conclusion

In this study, an unresolved SPH-DEM coupled model is proposed for AWJ study. The water-jet and targeted materials are modelled by SPH method, and the abrasive particles are modelled by DEM method. The capability of the coupled model in predicting ductile and brittle surface erosion behaviour is verified by comparing with the impact experiment results. The conclusions are summarized as follows:

1. For ductile materials, the erosion mechanism of AWJ is the material failure caused by plastic strain accumulation. The erosion process is divided into three stages: plastic strain accumulation, erosion crater formation and stable erosion. The crater depth $C_d$ increases linearly with the incident velocity $v_{jet}$, while the crater width $C_w$ tends to a stable value. The abrasive mass flow rate $M$ has a great influence on $C_w$. The crater profile changes from U-shaped to V-shaped with the increase of $M$, so the erosion rate and the crater size cannot be infinite improved by increasing $M$.
2. For brittle materials, the erosion mechanism of AWJ is the propagation and diffusion of cracks inside the material caused by repeated impact of abrasive particles. The erosion process is divided into two stages: erosion crater formation and stable erosion. The crater depth $C_d$ and crater width $C_w$ basically increase linearly with the incident velocity $v_{jet}$., and the number and size of cracks inside the material also increase significantly. The abrasive mass flow rate $M$ has a great influence on $C_d$. The crater profile changes from V-shaped to U-shaped with the increase of $M$. There is a threshold $M_{cri}$. When $M < M_{cri}$, $C_d$ increases linearly with $M$. When $M > M_{cri}$, radial cracks appear at the crater bottom. The material mass loss and $C_d$ increase significantly, resulting in the material fragmentation.

## Data availability

Data sets generated during the current study are available from the corresponding author on reasonable request.

Received: 16 July 2024; Accepted: 18 October 2024
Published online: 30 October 2024

## References


1. Hashish, M. A model study of metal cutting with abrasive water jets[J]. *J. Eng. Mater. Technol.* **106**, 88–100 (1984).
2. Liu, H. T. Waterjet technology for machining fine features pertaining to micromachining[J]. *J. Manuf. Process.* **12** (1), 8–18 (2010).
3. Tirumala, D., Gajjela, R. & Das, R. ANN and RSM approach for modelling and multi objective optimization of abrasive water jet machining process[J]. *Decis. Sci. Lett.* **7** (4), 535–548 (2018).
4. Gong, W. J., Wang, J. M. & Gao, N. Numerical simulation for abrasive water jet machining based on ALE algorithm[J]. *Int. J. Adv. Manuf. Technol.* **53** (1–4), 247–253 (2011).
5. Maniadaki, K. *et al*. A finite element-based model for pure waterjet process simulation[J]. *Int. J. Adv. Manuf. Technol.* **31**, 933–940 (2007).
6. Hsu, C. Y. et al. A numerical study on high-speed water jet impact[J]. *Ocean Eng.* **72**, 98–106 (2013).
7. Ma, L., Bao, R. H. & Guo, Y. M. Waterjet penetration simulation by hybrid code of SPH and FEA[J]. *Int. J. Impact Eng.* **35** (9), 1035–1042 (2008).
8. Junkar, M. *et al*. Finite element analysis of single-particle impact in abrasive water jet machining[J]. *Int. J. Impact Eng.* **32** (7), 1095–1112 (2006).
9. Wang, J. M., Gao, N. & Gong, W. J. Abrasive waterjet machining simulation by coupling smoothed particle hydrodynamics/finite element method[J]. *Chin. J. Mech. Eng.* **23** (5), 568–573 (2010).
10. Liu, S. Y. *et al*. Rock breaking of conical cutter with assistance of front and rear water jet[J]. *Tunn. Undergr. Space Technol.* **42**, 78–86 (2014).
11. Liu, S. Y., Chen, J. F. & Liu, X. H. Rock breaking by conical pick assisted with high pressure water jet[J]. *Adv. Mech. Eng.* **6**, 868041 (2014).
12. Jiang, H. X. et al. Numerical simulation of rock fragmentation under the impact load of water jet[J]. *Shock Vib.*, **2014**(1): 219489 .
13. Jiang, H. X., Liu, Z. H. & Gao, K. D. Numerical simulation on rock fragmentation by discontinuous water-jet using coupled SPH/FEA method[J]. *Powder Technol.* **312**, 248–259 (2017).
14. Ren, F. S., Fang, T. C. & Cheng, X. Z. Theoretical modeling and experimental study of rock-breaking depth in particle jet impact drilling process[J]. *J. Petrol. Sci. Eng.* **183**, 106419 (2019).
15. Ren, F. S., Fang, T. C. & Cheng, X. Z. Study on rock damage and failure depth under particle water-jet coupling impact[J]. *Int. J. Impact Eng.* **139**, 103504 (2020).
16. Fang, T. C. *et al*. Progress and development of particle jet drilling speed-increasing technology and rock-breaking mechanism for deep well[J]. *J. Petroleum Explor. Prod. Technol.* **12** (6), 1697–1708 (2022).
17. Takaffoli, M. & Papini, M. Material deformation and removal due to single particle impacts on ductile materials using smoothed particle hydrodynamics[J]. *Wear*. **274**, 50–59 (2012).
18. Takaffoli, M. & Papini, M. Numerical simulation of solid particle impacts on Al6061-T6 part I: three-dimensional representation of angular particles[J]. *Wear*. **292**, 100–110 (2012).
19. Hadavi, V. & Papini, M. Numerical modeling of particle embedment during solid particle erosion of ductile materials[J]. *Wear*. **342**, 310–321 (2015).
20. Peng, C. *et al*. A fully resolved SPH-DEM method for heterogeneous suspensions with arbitrary particle shape[J]. *Powder Technol.* **387**, 509–526 (2021).
21. Joubert, J. C. *et al*. 3D gradient corrected SPH for fully resolved particle–fluid interactions[J]. *Appl. Math. Model.* **78**, 816–840 (2020).
22. Hashemi, M. R., Fatehi, R. & Manzari, M. T. SPH simulation of interacting solid bodies suspended in a shear flow of an Oldroyd-B fluid[J]. *J. Nonnewton. Fluid Mech.* **166**, 1239–1252 (2011).
23. Shi, C. Q. *et al*. Numerical simulation of landslide-generated waves using a soil–water coupling smoothed particle hydrodynamics model[J]. *Adv. Water Resour.* **92**, 130–141 (2016).
24. Robinson, M., Ramaioli, M. & Luding, S. Fluid–particle flow simulations using two-way-coupled mesoscale SPH–DEM and validation[J]. *Int. J. Multiph. Flow*. **59**, 121–134 (2014).
25. Jo, Y. B. *et al*. GPU-based SPH-DEM method to examine the three-phase hydrodynamic interactions between Multiphase Flow and Solid Particles[J]. *Int. J. Multiph. Flow*. **153**, 104125 (2022).
26. Wu, K. *et al*. An integrated particle model for fluid–particle–structure interaction problems with free-surface flow and structural failure[J]. *J. Fluids Struct.* **76**, 166–184 (2018).
27. Sun, X. S., Sakai, M. & Yamada, Y. Three-dimensional simulation of a solid–liquid flow by the DEM–SPH method[J]. *J. Comput. Phys.* **248**, 147–176 (2013).
28. Yu, R. *et al*. A coupled SPH–DEM model for erosion process of solid surface by abrasive water-jet impact[J]. *Comput. Part. Mech.* **10** (5), 1093–1112 (2023).
29. Cundall, P. A. & Strack, O. D. L. A discrete numerical model for granular assemblies[J]. *Geotechnique*. **29** (1), 47–65 (1979).
30. Liu, C., Yu, Z. X. & Zhao, S. C. A coupled SPH-DEM-FEM model for fluid-particle-structure interaction and a case study of Wenjia gully debris flow impact estimation[J]. *Landslides*. **18** (7), 2403–2425 (2021).
31. Norouzi, H. R. *et al*. *Coupled CFD-DEM Modeling: Formulation, Implementation and Application to Multiphase flows[M]*20–47 (Wiley, 2016).
32. Xu, W. J., Dong, X. Y. & Ding, W. T. Analysis of fluid-particle interaction in granular materials using coupled SPH-DEM method[J]. *Powder Technol.* **353**, 459–472 (2019).
33. Zhang, S. et al. Simulation of solid–fluid mixture flow using moving particle methods[J]. *J. Comput. Phys.* **228** (7), 2552–2565 (2009).
34. Dong, X. W. *et al*. Modeling, simulation, and analysis of the impact(s) of single angular-type particles on ductile surfaces using smoothed particle hydrodynamics[J]. *Powder Technol.* **318**, 363–382 (2017).
35. Liu, G. R. & Liu, M. B. *Smoothed Particle Hydrodynamics: A Meshfree Particle method[M].Singapore*102–120 (World Scientific, 2004).
36. Dong, X. W. *et al*. A smoothed particle hydrodynamics (SPH) model for simulating surface erosion by impacts of foreign particles[J]. *Tribol. Int.* **95**, 267–278 (2016).
37. Du, M. C. *et al*. Experimental and simulation study on the influence factors of abrasive water jet machining ductile materials[J]. *Energy Rep.* **8**, 11840–11857 (2022).
38. Monaghan, J. J. & Lattanzio, J. C. A refined particle method for astrophysical problems[J]. *Astron. Astrophys.* **149**, 135–143 (1985).
39. Anderson, T. B. & Jackson, R. Fluid mechanical description of fluidized beds. Equations of motion[J]. *Industrial Eng. Chem. Fundamentals*. **6** (4), 527–539 (1967).
40. He, Y. *et al*. A GPU-based coupled SPH-DEM method for particle-fluid flow with free surfaces[J]. *Powder Technol.* **338**, 548–562 (2018).
41. Menikoff, R. Complete Mie-Gruneisen equation of state [R]. Los Alamos National Lab.(LANL), Los Alamos, NM (United States), (2016).
42. Liu, X. H., Liu, S. Y. & Ji, H. F. Numerical research on rock breaking performance of water jet based on SPH[J]. *Powder Technol.* **286**, 181–192 (2015).
43. Lo, E. Y. M. & Shao, S. D. Simulation of near-shore solitary wave mechanics by an incompressible SPH method[J]. *Appl. Ocean Res.* **24** (5), 275–286 (2002).
44. Monaghan, J. J. Smoothed particle Hydrodynamics[J]. *Annu. Rev. Astron. Astrophys.* **30** (1), 543–574 (1992).

45. Monaghan, J. J. Simulating free surface flows with SPH[J]. *J. Comput. Phys.* **110** (2), 399–406 (1994).
46. Randles, P. W. & Libersky, L. D. Smoothed particle hydrodynamics: some recent improvements and applications[J]. *Comput. Methods Appl. Mech. Eng.* **139** (1–4), 375–408 (1996).
47. Dong, X. W. *et al*. Smoothed particle hydrodynamics (SPH) simulation of impinging jet flows containing abrasive rigid bodies[J]. *Comput. Part. Mech.* **6**, 479–501 (2019).
48. Johnson, G. R. & Cook, W. H. Fracture characteristics of three metals subjected to various strains, strain rates, temperatures and pressures[J]. *Eng. Fract. Mech.* **21** (1), 31–48 (1985).
49. Piao, M. J. et al. Characterization of hardening behaviors of 4130 steel, OFHC Copper, Ti6Al4V alloy considering ultra-high strain rates and high temperatures[J]. *Int. J. Mech. Sci.* **131**, 1117–1129 (2017).
50. Holmquist, T. J. & Johnson, G. R. A computational constitutive model for glass subjected to large strains, high strain rates and high pressures[J]. *J. Appl. Mech.* **78** (5), 051003 (2011).
51. Holmquist, T. J. & Johnson, G. R. Characterization and evaluation of silicon carbide for high-velocity impact. *J. Appl. Phys.* **97** (9), 093502 (2005).
52. Huang, H. X., Li, W. B. & Lu, Z. Y. Determination of Parameters of Johnson-Holmquist-II (JH-2) Constitutive Model for Red Sandstone[C]. J. Phys.: Conf. Ser. IOP Publishing, **2002** (1), 012071. (2021).
53. Wang, J. X., Yin, Y. & Esmaieli, K. Numerical simulations of rock blasting damage based on laboratory-scale experiments[J]. *J. Geophys. Eng.* **15** (6), 2399–2417 (2018).
54. Shepard, D. A two-dimensional interpolation function for irregularly-spaced data[C]. Proceedings of the 1968 23rd ACM national conference. 517–524. (1968).
55. Wen, C. Y. & Yu, Y. H. Mechanics of Fluidization[J]. *Chem. Eng. Prog Symp. Ser.* **62**, 100–111 (1966).
56. Mao, Z. R., Liu, G. R. & Dong, X. W. A comprehensive study on the parameters setting in smoothed particle hydrodynamics (SPH) method applied to hydrodynamics problems[J]. *Comput. Geotech.* **92**, 77–95 (2017).
57. Yu, R. *et al*. Improved smoothed particle hydrodynamics (SPH) model for simulation of abrasive water-jet (AWJ)[J]. *Int. J. Comput. Methods*. **20** (06), 2143002 (2023).
58. Anwar, S., Axinte, D. A. & Becker, A. A. Finite element modelling of abrasive waterjet milled footprints[J]. *J. Mater. Process. Technol.* **213** (2), 180–193 (2013).



## Acknowledgements
This work was supported by National Natural Science Foundation of China [grant number 52075294 and U22A20204] and Natural Science Foundation of Shenzhen Municipality [grant number JCYJ20220530141006015].


## Author contributions
R.Y. and GN. H. conceived the experiments, R.Y. and WJ. Y. conducted the experiments and validated the numerical model, WJ. Y. and ZN.L. analyzed the results, GN. H. investigated the numerical model. All authors reviewed the manuscript.

## Declarations

## Competing interests
The authors declare no competing interests.

## Additional information
**Correspondence** and requests for materials should be addressed to G.H.

**Reprints and permissions information** is available at www.nature.com/reprints.

**Publisher's note** Springer Nature remains neutral with regard to jurisdictional claims in published maps and institutional affiliations.


**Open Access** This article is licensed under a Creative Commons Attribution-NonCommercial-NoDerivatives 4.0 International License, which permits any non-commercial use, sharing, distribution and reproduction in any medium or format, as long as you give appropriate credit to the original author(s) and the source, provide a link to the Creative Commons licence, and indicate if you modified the licensed material. You do not have permission under this licence to share adapted material derived from this article or parts of it. The images or other third party material in this article are included in the article's Creative Commons licence, unless indicated otherwise in a credit line to the material. If material is not included in the article's Creative Commons licence and your intended use is not permitted by statutory regulation or exceeds the permitted use, you will need to obtain permission directly from the copyright holder. To view a copy of this licence, visit http://creativecommons.org/licenses/by-nc-nd/4.0/.

© The Author(s) 2024